Joint local and teleseismic tomography in the central United States: exploring the mantle below the upper Mississippi Embayment and the Illinois Basin

Yu Geng[1], Christine A. Powell[1], and Arushi Saxena[1]

[1]University of Memphis

November 26, 2022

Abstract

Three-dimensional, high resolution crustal and upper mantle P- and S-wave velocity (Vp and Vs) models are presented for the central United States. The study utilizes local and teleseismic data recorded by the Northern Embayment Lithospheric Experiment stations, the New Madrid Seismic Network, the Earthscope Transportable Array, and the Ozark Illinois INdiana Kentucky Flexible Array. The Vp and Vs solutions are very similar and are well resolved in the depth range 40 to 400 km. Two anomalously slow regions are present below the Illinois Basin forming a northwest dipping low velocity zone (LVZ) extending from ˜200 to 400 km. Maximum anomaly magnitude in the LVZ reaches about -4 % and -5% for Vp and Vs, respectively. The LVZ appears to connect to a well-documented LVZ located below the northern Mississippi Embayment. As is the case for the northern Mississippi Embayment, the Illinois Basin velocity anomalies cannot be explained by elevated temperature alone and require elevated orthopyroxene content in addition to an increase in iron and water content. The need for additional orthopyroxene suggests that the LVZ is being produced by metasomatism of mantle rocks by hydrous, silica-rich fluids ascending from a slab fragment trapped in or near the transition zone. This supports previous interpretations for the existence of the LVZ below the Embayment. We suggest that the LVZs below the Mississippi Embayment and the Illinois Basin are linked to the presence of the large igneous province Hess plateau currently located below the central United States by inverse convection models.

Hosted file

`yugeng_supp_4submission.docx` available at https://authorea.com/users/111121/articles/605517-joint-local-and-teleseismic-tomography-in-the-central-united-states-exploring-the-mantle-below-the-upper-mississippi-embayment-and-the-illinois-basin

Joint local and teleseismic tomography in the central United States: exploring the mantle below the upper Mississippi Embayment and the Illinois Basin

Y. Geng[1], C. A. Powell[1], and A. Saxena[1,2]

[1]Center for Earthquake Research and Information, University of Memphis, Tennessee, USA.

[2]Department of Geological Sciences, University of Florida, Florida, USA.

Corresponding author: Yu Geng (ygeng1@memphis.edu)

Key Points:

- We present detailed 3D Vp and Vs models for the upper mantle beneath the central United States using data recorded by two FlexArrays.
- Two prominent low-velocity anomalies are imaged at 240 km and 370 km depth beneath the Illinois Basin.
- The origin of these anomalies is attributed in part to metasomatism of mantle rocks by silica rich fluids.

Abstract

Three-dimensional, high resolution crustal and upper mantle P- and S-wave velocity (Vp and Vs) models are presented for the central United States. The study utilizes local and teleseismic data recorded by the Northern Embayment Lithospheric Experiment (NELE) stations, the CERI New Madrid Seismic Network, the Earthscope Transportable Array (USArray), and the Ozark Illinois INdiana Kentucky Flexible Array (OIINK). The Vp and Vs solutions are very similar and are well resolved in the depth range 40 to 400 km. Two anomalously slow regions are present below the Illinois Basin forming a northwest dipping low velocity zone (LVZ) extending from ~200 to 400 km. Maximum anomaly magnitude in the LVZ reaches about -4 % and -5% for Vp and Vs, respectively. The LVZ appears to connect to a well-documented LVZ located below the northern Mississippi Embayment. As is the case for the northern Mississippi Embayment, the Illinois Basin velocity anomalies cannot be explained by elevated temperature alone and require elevated orthopyroxene content in addition to an increase in iron and water content. The need for additional orthopyroxene suggests that the LVZ is being produced by metasomatism of mantle rocks by hydrous, silica-rich fluids ascending from a slab fragment trapped in or near the transition zone. This supports previous interpretations for the existence of the LVZ below the Embayment. We suggest that the LVZs below the Mississippi Embayment and the Illinois Basin are linked to the presence of the large igneous province Hess plateau currently located below the central United States by inverse convection models.

Plain Language Summary

We present three-dimensional, high-resolution velocity models from the Earth's surface to 410 km depth under the central United States. Our study utilizes seismic tomography – a technique that images the velocity structure of the Earth using seismic waves that traveled from earthquake

sources to seismic stations. Travel-time data recorded by several seismic arrays (dense deployments of seismic stations) were acquired to increase the resolution of our model. In the resultant model, compressional wave and shear wave velocities are similar and are well-resolved in the depth range 40 to 400 km. An anomalously slow region is present below the Illinois Basin that dips to the northwest and extends to 400 km. The slow velocity cannot be explained by elevated temperature alone and requires an increase in iron and water content as well as high amounts of orthopyroxene. Elevated orthopyroxene suggests that the mantle rocks have been chemically altered due to fluids coming from a trapped slab fragment. We suggest that the low-velocity zone below the Illinois Basin is associated with the presence of a slab fragment containing the thick oceanic Hess plateau. According to several studies, the Hess plateau was subducted millions of years ago and is presently located underneath the central United States.

1 Introduction

The midcontinent of the United States is located far from a plate boundary but contains several concentrated areas of seismic activity. These include the New Madrid Seismic Zone (NMSZ), the Wabash Valley Seismic Zone (WVSZ), and the Ste. Genevieve Seismic Zone (SGSZ) (Figure 1). The presence of these zones poses a hazard to a region ill prepared for seismic activity. Understanding the underlying reason for the existence of these zones can help answer fundamental questions such as the expected longevity of the zones and the recurrence interval of large earthquakes. The Reelfoot Rift, located within the Mississippi Embayment (ME), hosts the NMSZ. Three large (Mw>7) NMSZ earthquakes occurred in 1811-1812 (Nuttli, 1973; Johnston, 1966; Hough and Page, 2011; Van Arsdale and Cupples, 2013) and paleoseismic evidence indicates a repeat time of about 500 years for earthquakes of similar magnitude (Tuttle

et al., 2002; Van Arsdale et al., 2012). The WVSZ and the SGSZ, located to the northeast and northwest of the NMSZ, respectively, may have the same potential for creating large earthquakes. The WVSZ and the NMSZ may be mechanically coupled; numerical modeling indicates that stress transfer following the 1811-1812 New Madrid earthquakes may be loading faults in the Wabash zone (Li et al., 2005, 2007; Mueller et al., 2004). However, the mechanism of stress coupling between seismic zones remains enigmatic. Several models have been proposed for the existence of the NMSZ (e.g. Kenner and Segall, 2000; Thybo et al., 2000; Pollitz et al., 2001), but none has reached wide acceptance. Even less is known about the origins of the WVSZ and the SGSZ.

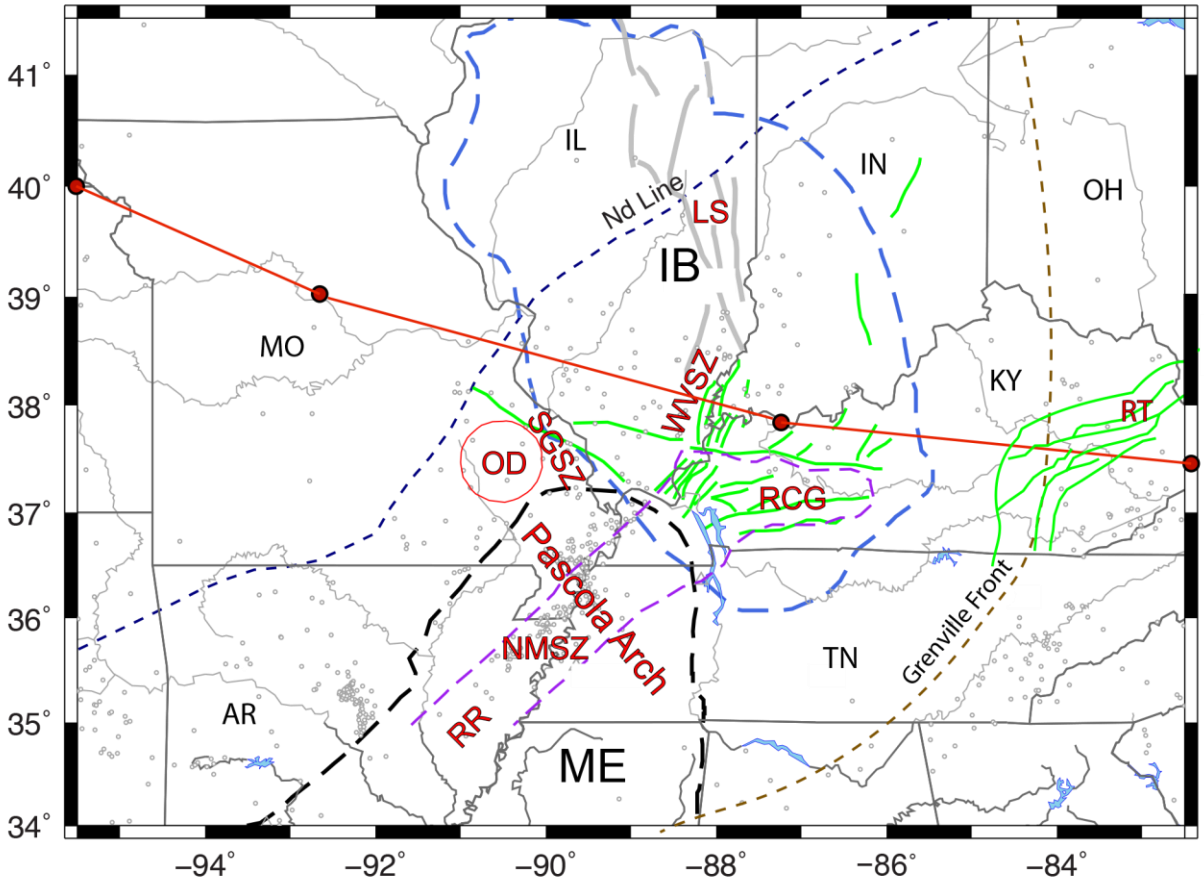

Figure 1. Major features in the study area. Solid green lines and solid gray lines delineate fault traces and fold systems, respectively. Purple dashed line marks the boundary of the Reelfoot Rift (RR). Dashed blue line and dashed black line delineate the boundaries of the Illinois Basin (IB) and the Mississippi Embayment (ME), respectively. Red line marks the path of a Cretaceous-age hotspot proposed by Chu et al. (2013). Ozark Dome (OD); Rome Trough (RT); Rough Creek Graben (RCG), New Madrid Seismic Zone (NMSZ); Ste. Genevieve Seismic Zone (SGSZ); Wabash Valley Seismic Zone (WVSZ); La Salle fold system (LS). Gray dots are epicenters of M≥2.0 earthquakes that occurred between January 1974 and December 2014 from the International Seismological Centre (ISC) catalog. AR: Arkansas; MO: Missouri; IL: Illinois: IN: Indiana; OH: Ohio; KY: Kentucky; TN: Tennessee.

Discoveries of anomalous mantle velocity structure in the central United States (CUS) made possible by deployment of the Earthscope Transportable Array, the Northern Embayment Lithosphere Experiment (NELE) FlexArray and the Ozarks-Illinois-INdiana-Kentucky (OIINK) FlexArray (Figure 2) suggest a causative link between mantle velocity heterogeneity and intraplate seismic zones. Several studies have indicated the presence of a low velocity zone (LVZ) below the Reelfoot Rift (Chen et al., 2014; Pollitz and Mooney, 2014; Chen et al., 2016; Nyamwandha et al., 2016). This LVZ is unique to the Reelfoot Rift; similar LVZs are not associated with other ancient CUS rift structures such as the Mid-Continent Rift (Pollitz and Mooney, 2014).

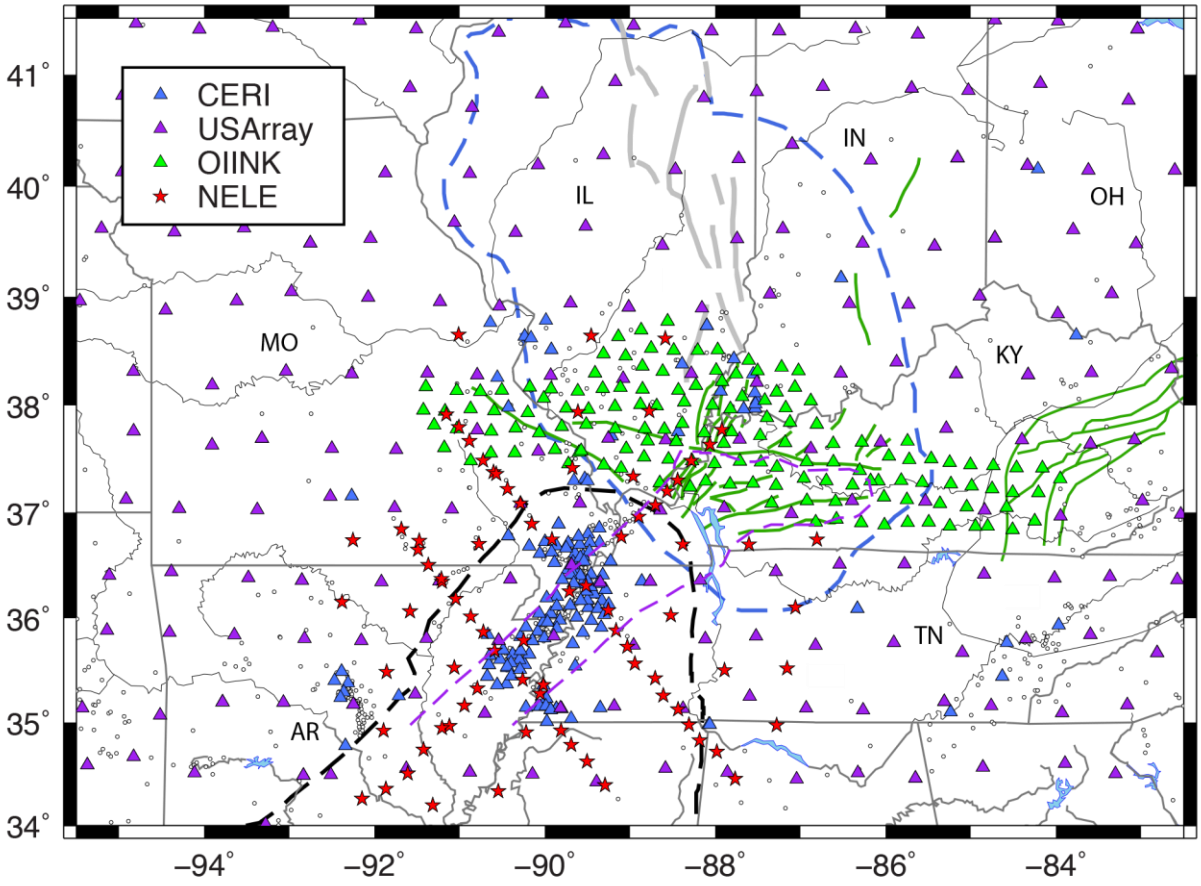

Figure 2. The 594 stations from the NELE, CERI, OIINK, and TA seismic networks used in our study. Stations were operational in all or part of the period January 2011 to December 2015.

The highest resolution upper mantle velocity models below the Reelfoot Rift are found in Nyamwandha et al. (2016) and are based on local and teleseismic earthquakes recorded by TA stations and the NELE broadband station deployment. P- and S-wave velocity models (Vp and Vs models) are determined in this study and indicate that the LVZ dips to the SW and extends from about 100 km below the NMSZ to a depth of at least 250 km below Arkansas. An unusual result of this study is that the Vp and Vs anomalies within the LVZ have similar magnitudes; normally, Vs is more strongly affected by variations in temperature, composition, and fluid

content than Vp (Cammarano et al., 2003; Lee, 2003; Jacobsen et al., 2004). A possible explanation for the similar magnitude anomalies is orthopyroxene enrichment which is usually attributed to the presence of a subducted slab (e.g. Wagner et al., 2008). Nyamwandha et al. (2016) attributed the LVZ to the metasomatic alteration of mantle rocks due to the assent of hot, hydrous fluids from a segment of the Farallon slab trapped in the transition zone. An analogous situation exists below the North China Craton where fluids rising from the trapped Pacific slab are eroding the sub continental lithosphere (e.g. Kusky et al., 2007). Zhan et al. (2016) discussed the importance of the LVZ below the Reelfoot Rift for the generation of earthquakes; the weak, low viscosity zone will transfer stress to the upper crust, making the NMSZ a favorable location for earthquake activity in the presence of additional triggering events such as deep erosion by glacial melting. The concept of stress amplification in the upper crust due to the presence of a weak lower crust or upper mantle is the basis of a model for the NMSZ that successfully reproduces important observations such as the recurrence interval for large earthquakes and minimal surface strain rates (Kenner and Segall, 2000). Investigating the upper mantle below the Illinois Basin may reveal a connection between mantle velocity structure and the generation of earthquakes in the SGSZ and the WVSZ.

In this study, we present 3-D Vp and Vs models for the upper mantle that extend the results of Nyamwandha et al. (2016) northward into the Illinois Basin. Our models include the mantle below the WVSZ and the SGSZ. We use the same stations as Nyamwandha et al. (2016) and stations deployed by the OIINK FlexArray experiment (Yang et al., 2014). The accessibility of high-resolution seismic data from both FlexArray experiments offers an opportunity to address long-standing scientific questions such as: What is the relationship between the Reelfoot Rift and the Illinois Basin? Is the mantle below the two regions distinctly different? What is the

128 possible influence of mantle velocity structure on the seismic zones? Our study will provide
129 insights into the connections between mantle velocity structure and the seismic zones, and
130 between the Illinois Basin and the Reelfoot Rift.

131 **2 Geologic and tectonic setting**

132 2.1 The North American Midcontinent

133 Much of the CUS is located within the ancient North American craton. The Precambrian
134 basement was developed by accretion of exotic terranes to the southeastern margin of the
135 Archean lithosphere during growth of the continent. A 1.55 to 1.35 Ga episode of felsic intrusion
136 and eruption produced the Eastern Granite-Rhyolite Province (EGRP) (Bickford et al., 2015).
137 The EGRP lies below our entire study area. The origin of the EGRP is enigmatic but possibly
138 involved basaltic underplating and crustal melting along an active plate margin extending from
139 eastern Canada, across the CUS, and into the current southwestern US (Bickford et al., 2015).
140 Additional lithosphere was added to the eastern and southern portions of the continent during the
141 ~ 1.1 Ga Grenville orogeny. The Grenville orogeny is associated with the formation of super
142 continent Rodinia. The location of the Grenville front in the CUS probably lies to the east and
143 south of our study area (Figure 1), but Grenville flat slab subduction may have extended below
144 the Illinois Basin (Bedle and van der Lee, 2006). Extension occurred in the CUS during the
145 Grenville orogeny, producing the Midcontinent Rift and other extensional structures (Whitmeyer
146 and Karlstrom, 2007). The breakup of Rodinia in the Late Precambrian and Early Cambrian
147 fragmented the midcontinent, leading to the formation of rift and transform basement structures,
148 including the Reelfoot Rift, Rough Creek Graben, and the Rome Trough (Thomas et al., 2006)
149 (Figure 1). Subsequently, intracratonic-scale domes, arches, and basins formed in the region as a

consequence of the Appalachian and Ouachita orogenies. Uplift of the Pascola Arch at the end of the Permian effectively isolated the Illinois Basin from the Reelfoot Rift and the Mississippi Embayment.

2.2 Cratonic basins

The formation of cratonic basins represents an example of long-term intraplate deformation within the North American plate. There is no generally accepted mechanism for the formation of the basins although several hypotheses have been proposed to explain their origin. Much debate focuses on the origin of the Illinois Basin. Most of the basin fill is Cambrian through Pennsylvanian strata deposited as the basin subsided in the Paleozoic. A NE trending boundary (the Nd line, Figure 1) cuts across the basin, separating pre-1.6 Ga crust to the NW from younger, post-1.6 Ga crust to the SE. The line may separate older crust accreted during the Mazatzal orogeny from younger crust to the SE (Bickford et al., 2015). The initial formation of the Illinois Basin may have been linked to the same deformational processes that formed the Reelfoot Rift and the Rough Creek Graben (e.g. Marshak and Paulsen, 1996). Yang et al. (2017) found very thick crust (up to ~ 60 km) below the basin to the SE of the Nd line in a receiver function study, suggesting that the presence of the older thick crust may have influenced the subsidence of the basin. An abrupt change in crustal thickness occurs at the border between the Illinois Basin and the Ozark Dome. Yang et al. (2017) argued that the crustal thickness variations occurred prior to the formation of the basin and presented several hypotheses for the thick crust in the central and southern portions of the basin. These models involve processes at an active convergent margin, such as underthrusting, delamination, and magmatic underplating. Seismic reflectors have been observed in the basement and have been interpreted as the remnants of a

Proterozoic rhyolitic caldera complex or rift complex related to the thermal event that created the EGRP (McBride et al., 2003; Okure and McBride, 2006).

A prominent anticlinal structure, the La Salle deformation belt, trends northwest through the central Illinois Basin (delineated with solid gray lines in Figure 1). The La Salle belt is geologically complex, consisting of domes, synclines, anticlines, and monoclines (McBride, 1997). The folds are underlain by reverse faults that disrupt and offset intrabasement structures and offset the top of the Precambrian basement. McBride (1997) suggests that the deformation is similar to Rocky Mountain basement thrust generated folds but on a smaller scale. The southeastern end of the La Salle belt is connected to the northern boundary of the WVSZ (Figure 1). Moderate, upper crustal earthquakes located west of the La Salle belt have reverse and strike-slip mechanisms, suggesting reactivation of deep basement faults (McBride, 1997).

Previous studies provide insight into the mantle velocity structure below the Illinois Basin. A study using reprocessed seismic reflection data (Okure and McBride, 2006) reported mantle reflectivity beneath the Illinois basin, which indicates significant uppermost mantle heterogeneity relative to other parts of the United States. The mantle reflectivity defines an anomalous area that rests beneath the depocenter of the early Paleozoic Illinois Basin. A 3-D shear velocity model of the Illinois Basin (Bedle and van der Lee, 2006) contains a low velocity region extending from the base of the crust to about 90 km depth. Bedle and van der Lee (2006) attributed the slow velocity to the presence of a mantle wedge with hydrous minerals related to a Grenville age, fossilized flat slab. High crustal velocities beneath the southern Illinois Basin identified by Chen et al. (2016) support the interpretation that basin formation was influenced by the same rifting event that formed the Reelfoot Rift.

3 Data and methods

This study incorporates local and teleseismic earthquakes recorded by NELE, the New Madrid Seismic Network operated by the Center for Earthquake Research and Information (CERI), the Earthscope USArray (TA), and OIINK (Figure 2). The average spacing of the NELE stations is ~ 20 km. The NELE stations were deployed in two phases. The first phase was from September 2011 to October 2013 and consisted of four separate six-month deployments; the second phase began in July 2013 and finished in June 2015 and involved deployment of an additional 51 broadband stations. The OIINK Array has an average station spacing of ~ 25 km. It was divided into three phases that migrated from west to east. The first phase (July 2011 to June 2012) included 14 short-period and 9 broadband stations and went across the Mississippi River between Missouri and Illinois. The array expanded to 70 broadband seismic stations in the second phase and was deployed across southeastern Missouri and southern Illinois from June 2012 to late 2013. The final phase started in August 2013 and ended in October 2015 with stations deployed in southern Indiana and western Kentucky. Compared to the average spacing of TA stations, ~ 70 km, the involvement of NELE and OIINK stations dramatically increases the lateral resolution of the tomographic model in our study.

The dataset for the inversion consists of arrival times from local earthquakes and relative travel time residuals from teleseismic earthquakes recorded over five years (2011 to 2015). The first part of our dataset consists of 292 teleseismic events with $M \geq 5.5$ from 30° to 90°, selected to achieve as even an azimuthal coverage around the study area as possible. Arrival times were picked with the Automated and Interactive Measurement of Body-wave Arrival Times (AIMBAT) tool by Lou et al. (2013). The tool is based on multi-channel cross-correlation

(MCCC), and the initial phase marking part of the MCCC procedure is replaced with an iterative cross-correlation and stack (ICCS) algorithm.

The second part of the dataset is from Nyamwandha et al. (2016) and consists of 519 local and regional events with M≥2.0 and 282 teleseismic events (30° to 90° from the study area) with M≥5.5. Arrival times were recorded by the TA, CERI, and NELE networks. To fill in the gaps in the azimuth coverage of the above earthquakes, we also examined events within 160° to 180° from the study area for PKP arrivals. Three additional events that have 153 clear PKP arrivals in total were added after careful inspection. They are the Mw 6.4 Mid-Indian Ridge earthquake on October 4, 2013, the Mw 5.9 Southeast Indian Ridge earthquake on May 29, 2015, and the Mw 7.1 Southeast Indian Ridge earthquake on December 4, 2015 (Figure 3).

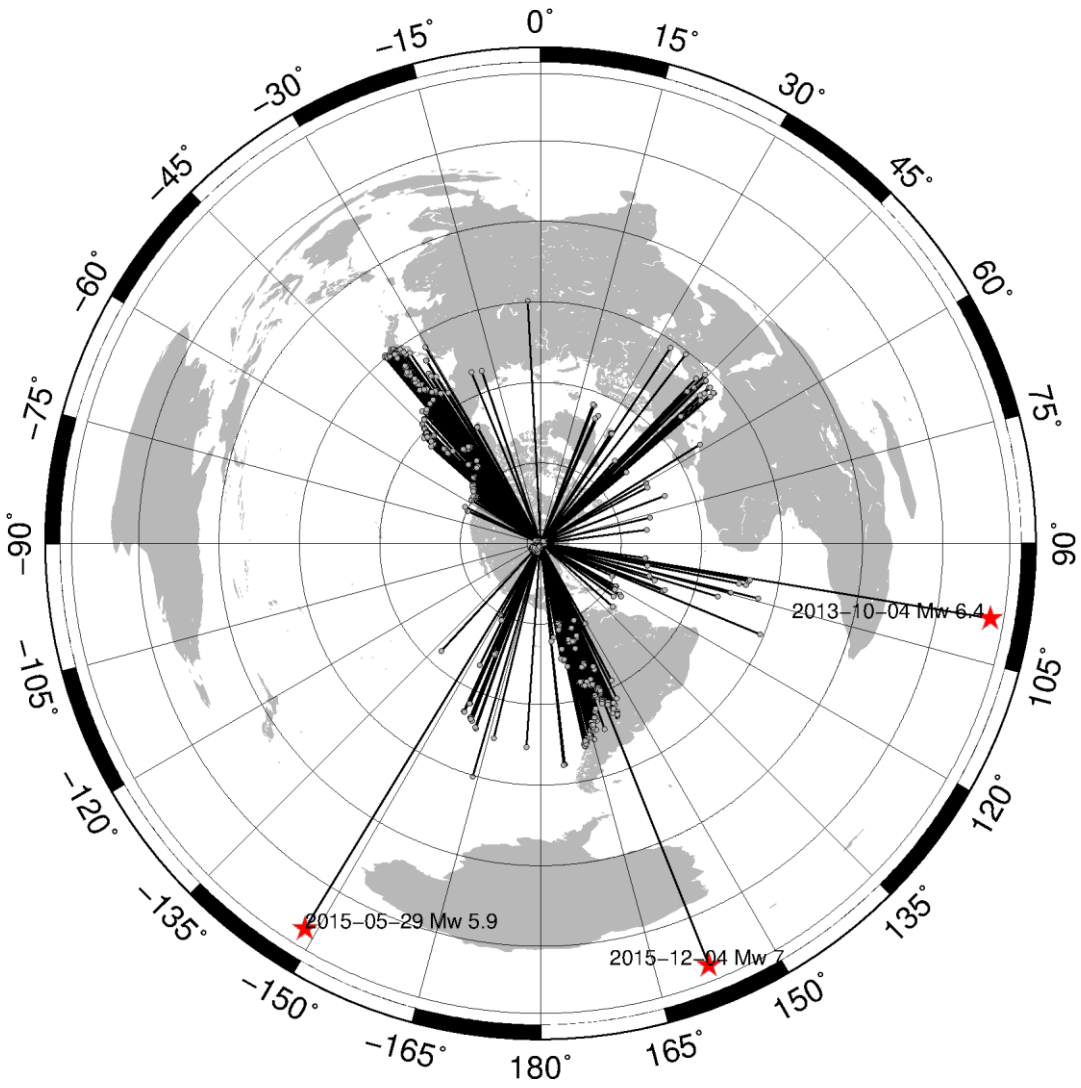

Figure 3. Azimuth coverage of the 1096 events used in the tomographic inversion. The dataset consists of 519 local and regional events with M≥2.0 and 577 teleseismic events with M≥ 5.5. Solid gray circles denote events with epicentral distances <90◦. Three events at epicentral distances of 160◦ to 180◦ are marked with red stars. They were acquired from the Incorporated Research Institutions for Seismology (IRIS).

The joint inversion method of Zhao et al. (1994), TOMOG3D, is used to obtain the 3-D Vp and Vs models of the crust and upper mantle. This technique uses a 3-D ray-tracing

algorithm for calculation of theoretical travel times and ray paths (Zhao et al., 1992, 1996). The code was developed to study detailed three-dimensional velocity structures (Zhao et al., 1992) and allows the introduction of discontinuities in the starting model. The depths to a discontinuity are expressed as 2-D grid nodes; at any location within the study area, the depth of the discontinuity can be calculated by linearly interpolating the depths at the surrounding four grid points.

For teleseismic events, relative traveltime residuals are calculated using the technique described in Zhao et al. (1994): (1) for each record, the travel time is converted into a residual by subtracting the theoretical travel time computed using the IASP91 model (Kennett and Engdahl, 1991). (2) for each earthquake, the mean residual value is removed from all records. Removal of average residuals effectively reduces the uncertainties introduced by hypocentral mislocations, origin times, and path effects outside of the modeling space (Zhao et al., 1994). The above dataset and processing methods produced a total of 16200 arrival times from local earthquakes and 53680 relative residuals from teleseismic earthquakes.

Following Chen et al. (2016), the starting Vp and Vs models are constructed by concatenating the Catchings (1999) crustal velocity model and the upper mantle portion of the IASP91 model (Figure 4a). The starting Vp/Vs model is obtained by dividing the starting Vp model by the starting Vs model (Figure 4b). The optimum damping and smoothing values were determined using the technique by Eberhart-Phillips (1986) and were presented in Supporting Information **Text S1**.

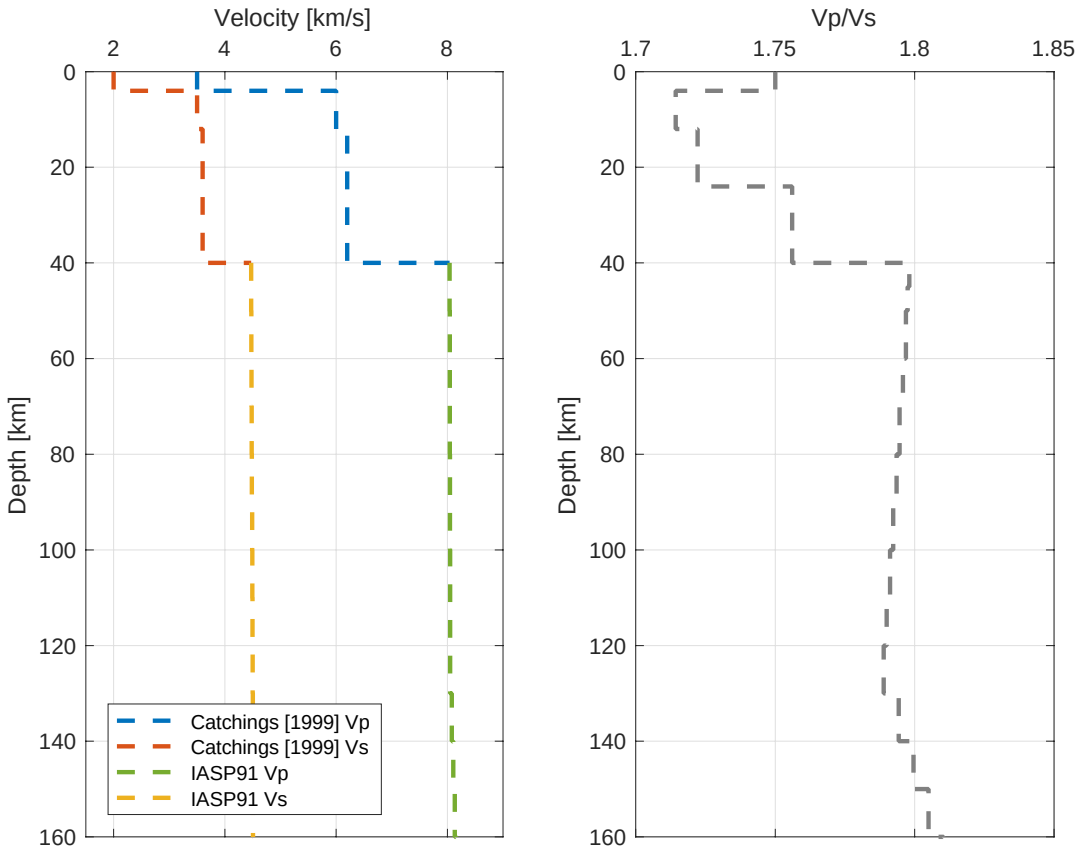

255

256 **Figure 4**. 1-D starting Vp and Vs models **(a)** and Vp /Vs model **(b)**. The upper 40 km is the
257 Catchings (1999) model obtained from a seismic refraction experiment in the Mississippi
258 Embayment. The portion below 40 km is the IASP91 model (Kennett and Engdahl, 1991). The
259 Vp /Vs model is obtained by dividing Vp by Vs at each depth.

260

261 **4 Results**

262 4.1 Checkerboard resolution test

263 The study area was parameterized with 50 km × 50 km grids horizontally and 16 vertical
264 layers from the surface to 600 km depth. The optimum horizontal grid spacing was found by

testing a range of node separations and determining the minimum RMS traveltime residual. In the vertical direction, five layers were set up for the crust, and 11 layers were set up for the mantle. The separation between these layers gradually increases with depth. The minimum number of observations at a grid point for it to be included in the inversion was set to 10.

Synthetic checkerboard models were created to investigate spatial resolution. Each checkerboard box consists of 2×2 grids horizontally and is therefore 100 km × 100 km in size. Across the boundary between adjacent boxes, a velocity contrast of 10% (±5%) was introduced. The above configuration divided the study area into ~ 13 checkerboard boxes in longitude and ~8 checkerboard boxes in latitude. Synthetic travel time data were computed for the checkerboard model using the ray-tracer in TOMOG3D. Random errors that lie between −0.5 sec and +0.5 sec were superimposed on the synthetic data in order to simulate picking errors in the real data. The synthetic data were inverted to recover the patterns in the input checkerboard model, using the same technique and the same source and station distributions as the real data inversion. In the output checkerboard models, all depth slices from 40 km to 400 km show well-recovered patterns (Figures 5 and 6). The recovered patterns diminish beneath 400 km because ray paths coming from teleseismic events become sparser below this depth. Patterns are not well-resolved in the upper 20 km because ray paths are nearly parallel to each other and at near-vertical incidence.

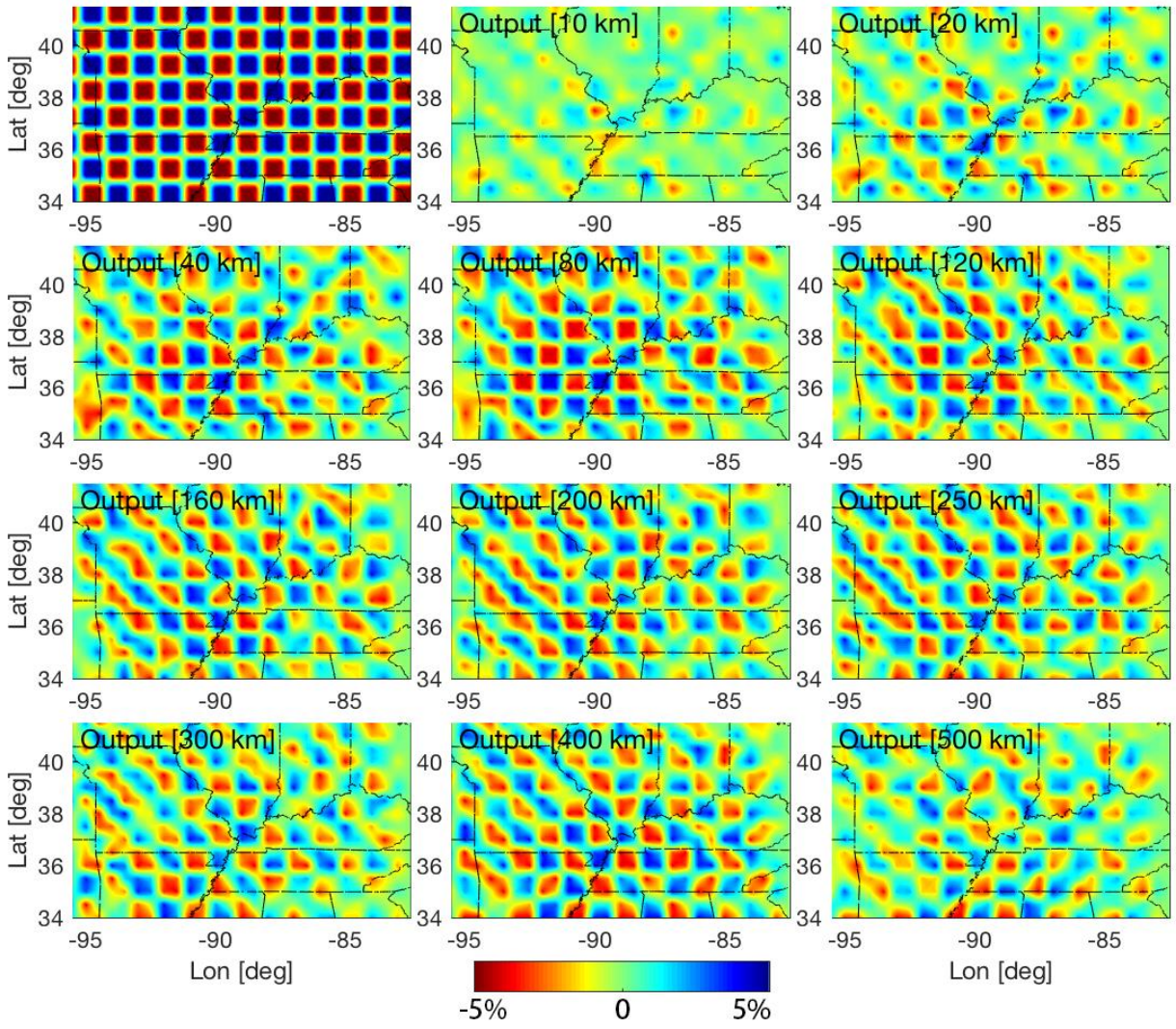

283

284 **Figure 5**. Input and output P-wave checkerboard models. Patterns at depths between 40 km to

285 400 km are well-recovered.

286

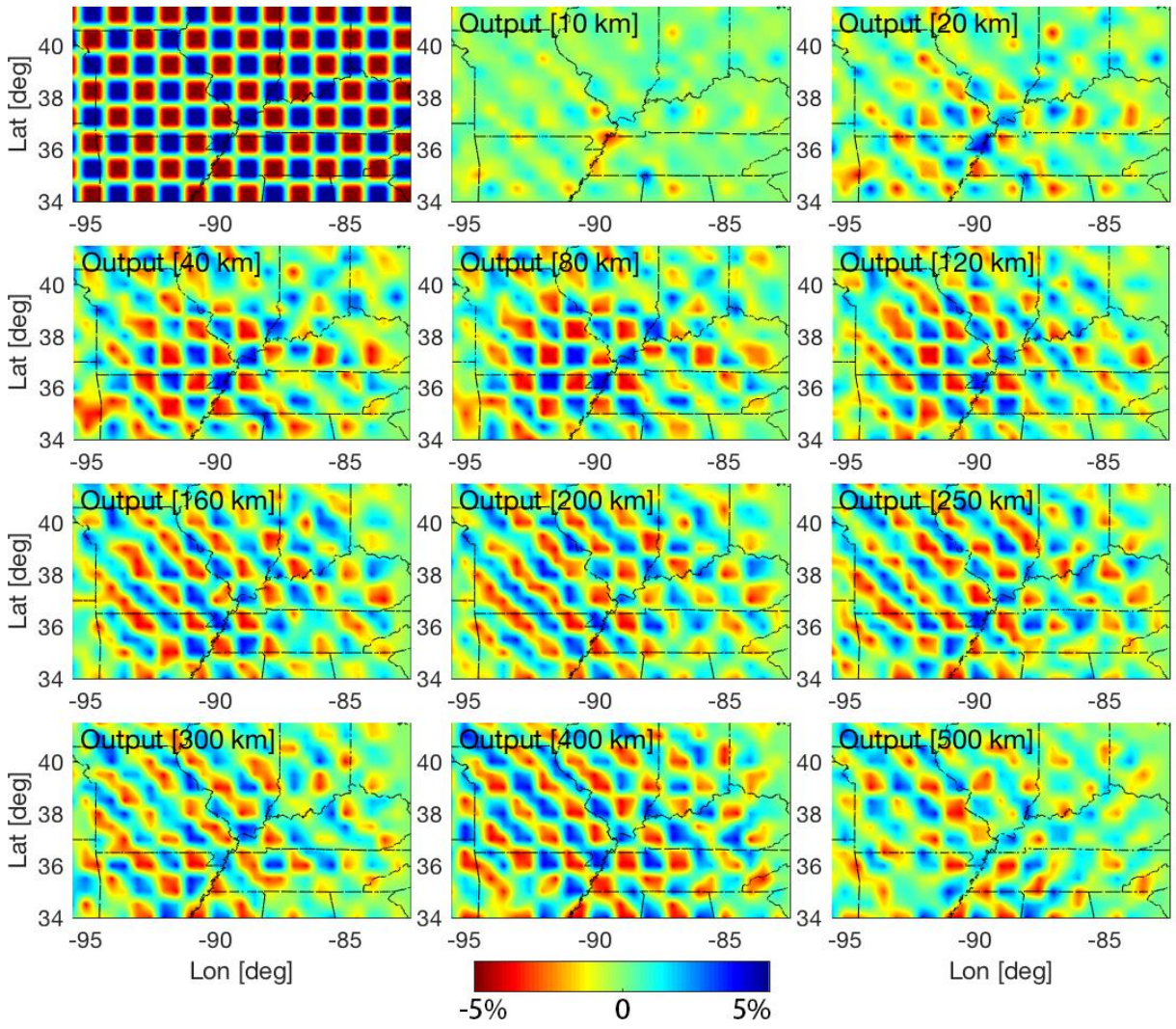

Figure 6. Input and output S-wave checkerboard models. The checkerboard recovery is comparable to the recovery found for the P-wave velocity solution.

4.2 Real data inversion

4.2.1 a priori data

For the real data inversion, we incorporated several datasets from previous studies as *a priori* constraints on major discontinuities in the Earth: sediment thickness, Moho depth, and depth to the 410 km discontinuity. The geometry of the sediment (Figure 7a) was extracted from the Central U.S. Velocity Model (CUSVM) (Ram´ırez-Guzm´an et al., 2012). The sediment of the ME consists mainly of post-Paleozoic deposits. Sediment thickness varies from < 1 km in the northern ME to 2 km in the southern ME. There is a high impedance contrast between the sediment and the bedrock, which makes it crucial to characterize the geometry of the sediment throughout the region (Ram´ırez-Guzm´an et al., 2012). The dataset for the 410 km discontinuity (Figure 7c) was obtained from Gao and Liu (2014). These authors used receiver functions to map depths to the 410 km and the 660 km discontinuities beneath the contiguous United States and adjacent areas. There are several datasets representing depths to the Moho (Ram´ırez-Guzm´an et al., 2012; Laske et al., 2013; McGlannan and Gilbert, 2016; Yang et al., 2017). After comparing the results using different crustal thickness models, the OIINK CUS Moho 2017 (Figure 7b) was included in our starting model to obtain the final tomographic images. Details of the comparison are presented in Supporting Information **Text S2**.

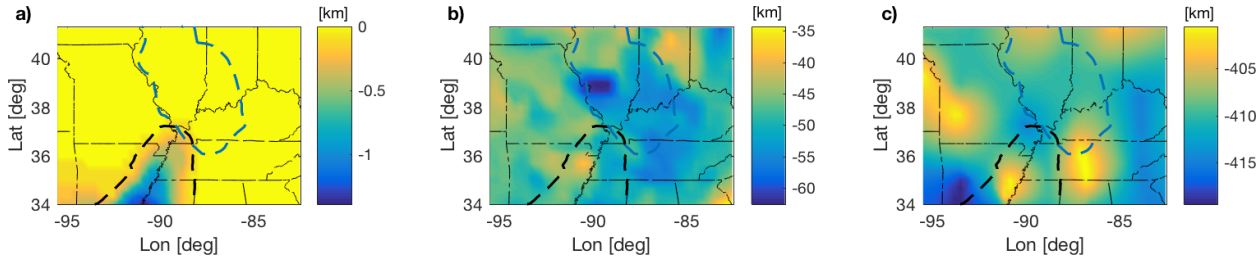

309 **Figure 7**. Datasets representing depths to the major discontinuities that have been included in the
310 starting model: **(a)** thickness of the sediment from the Central U.S. Velocity Model (Ram´ırez-
311 Guzm´an et al., 2012); **(b)** depths to the Moho from the OIINK CUS Moho 2017 (Yang et al.,
312 2017); **(c)** depths to the 410 km discontinuity (Gao and Liu, 2014). The boundaries of the Illinois
313 Basin and the Mississippi Embayment are delineated with a dashed blue line and a dashed black
314 line, respectively.

315

316 4.2.2 Vp and Vs models

317 The Vp and Vs models are presented in Figures 8 and 9 and were determined using the
318 optimum damping and smoothing parameters and selected *a priori* datasets. Four cross-sectional
319 views of the velocity models are presented in Figures 10 and 11: AA' and BB' are roughly
320 perpendicular to the Reelfoot Rift; CC' goes through the NMSZ and extends into the SGSZ; DD'
321 is parallel to the Reelfoot Rift and extends into the WVSZ. The Vp and Vs solutions are similar
322 at all depths. Vs anomaly magnitudes are larger than the Vp anomaly magnitudes for most of the
323 major mantle features resulting in positive Vp/Vs ratio perturbations (Figure 12).

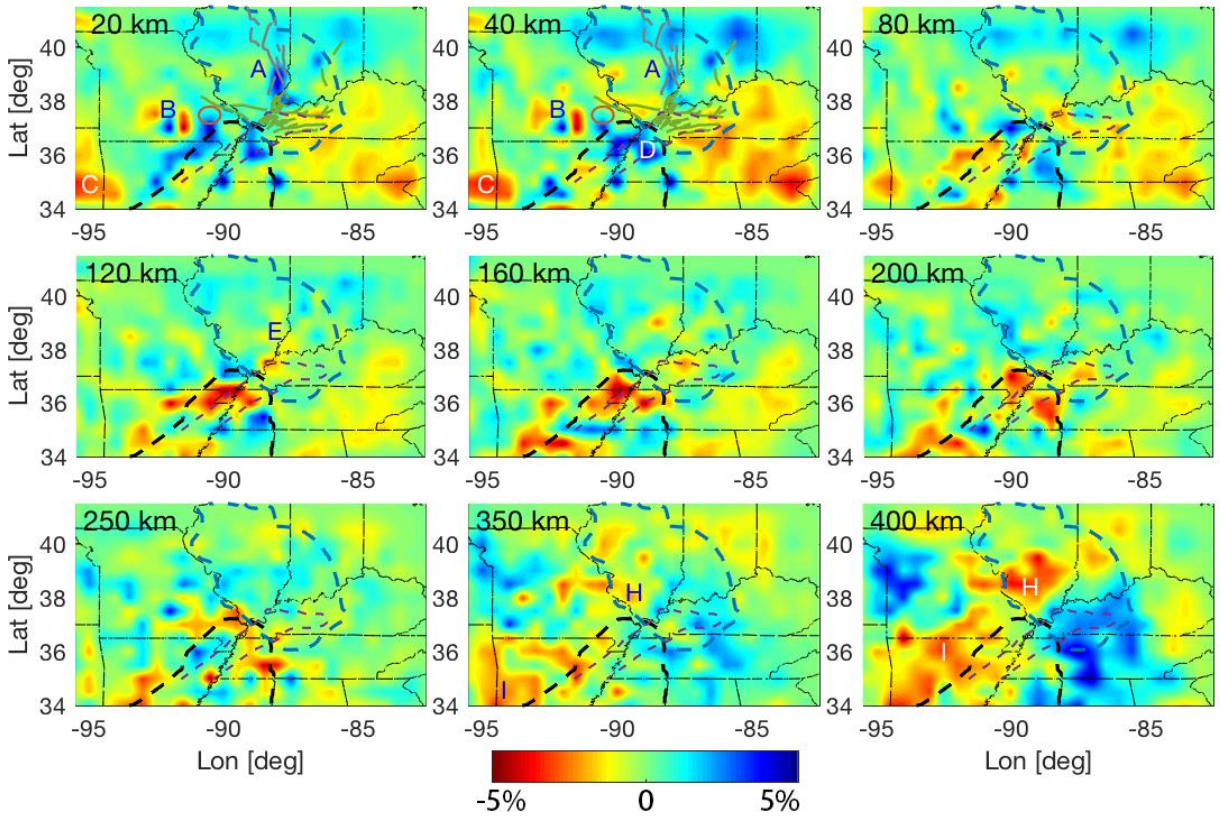

Figure 8. Horizontal slices through the Vp model. Fault traces and fold systems are delineated with solid green lines and solid gray lines, respectively. The Ozark Dome is delineated with an orange circle. Dashed purple line marks the boundary of the Reelfoot Rift. The boundaries of the Illinois Basin and the Mississippi Embayment are delineated with a dashed blue line and a dashed black line, respectively.

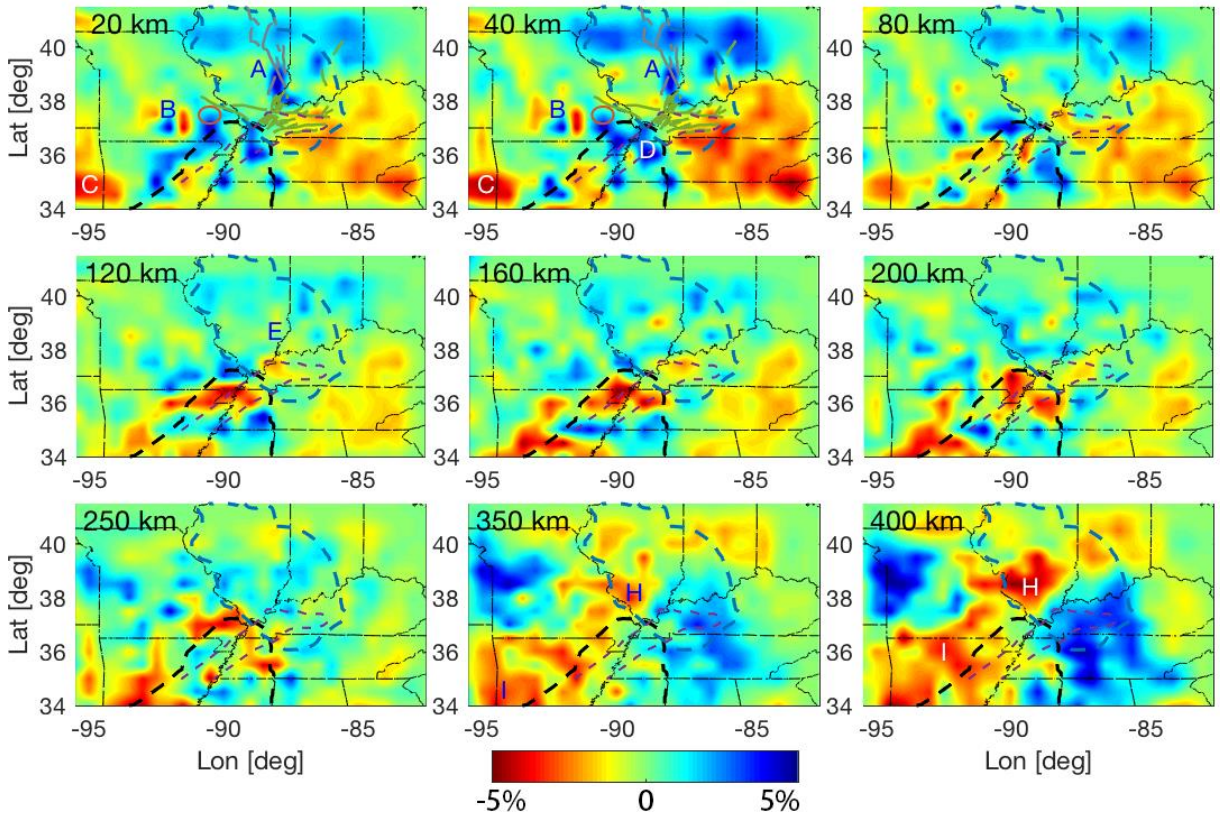

Figure 9. Horizontal slices of the output Vs model. Notations for major geology features are the same as those in Figure 8. Vs and Vp anomalies have a similar spatial distribution but, in most cases, the Vs anomalies have larger magnitudes.

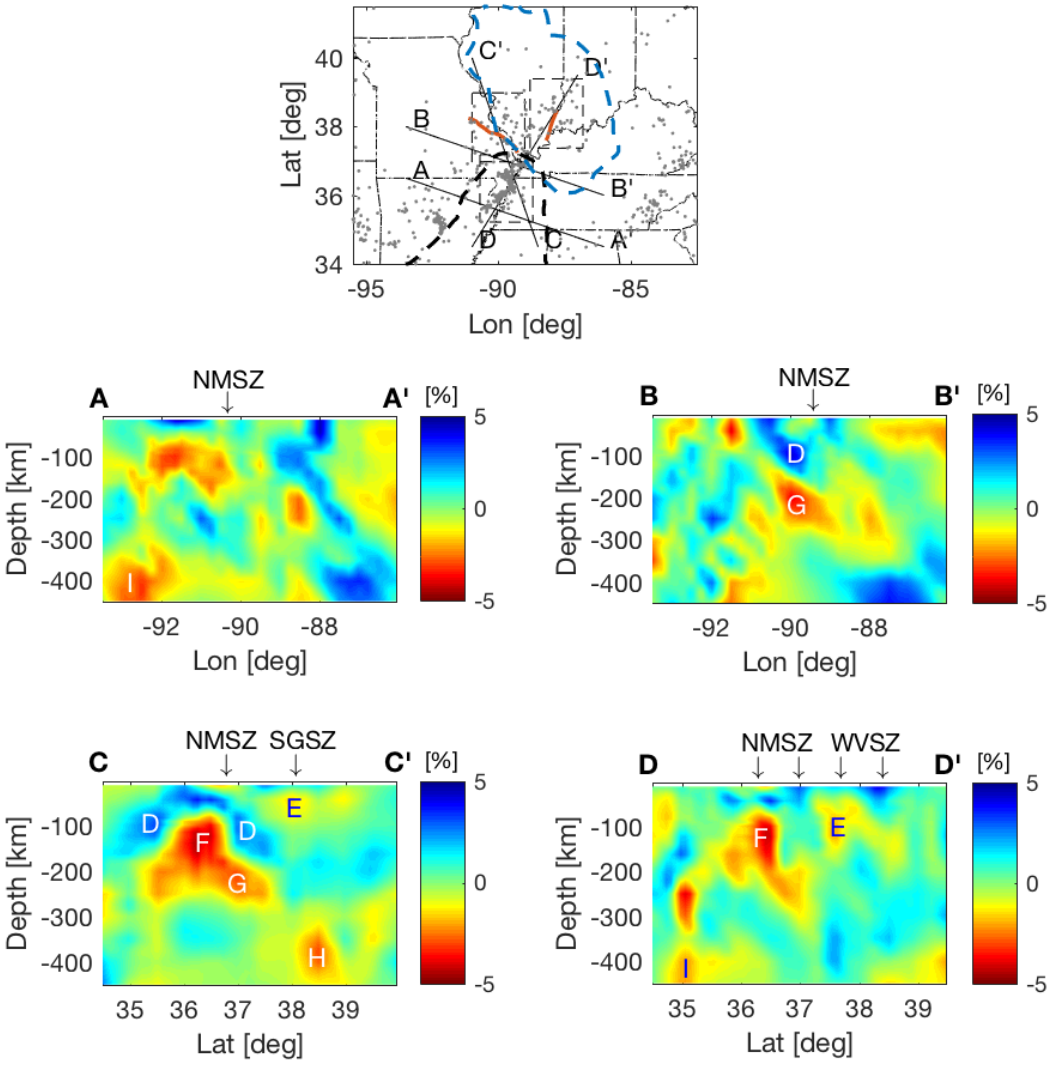

336

337 **Figure 10**. Vertical slices through the Vp model. On the map view, thick, orange lines indicate

338 the locations of the SGSZ (crossed by CC') and the WVSZ (crossed by DD'). AA', BB' and

339 DD' pass through the NMSZ.

340

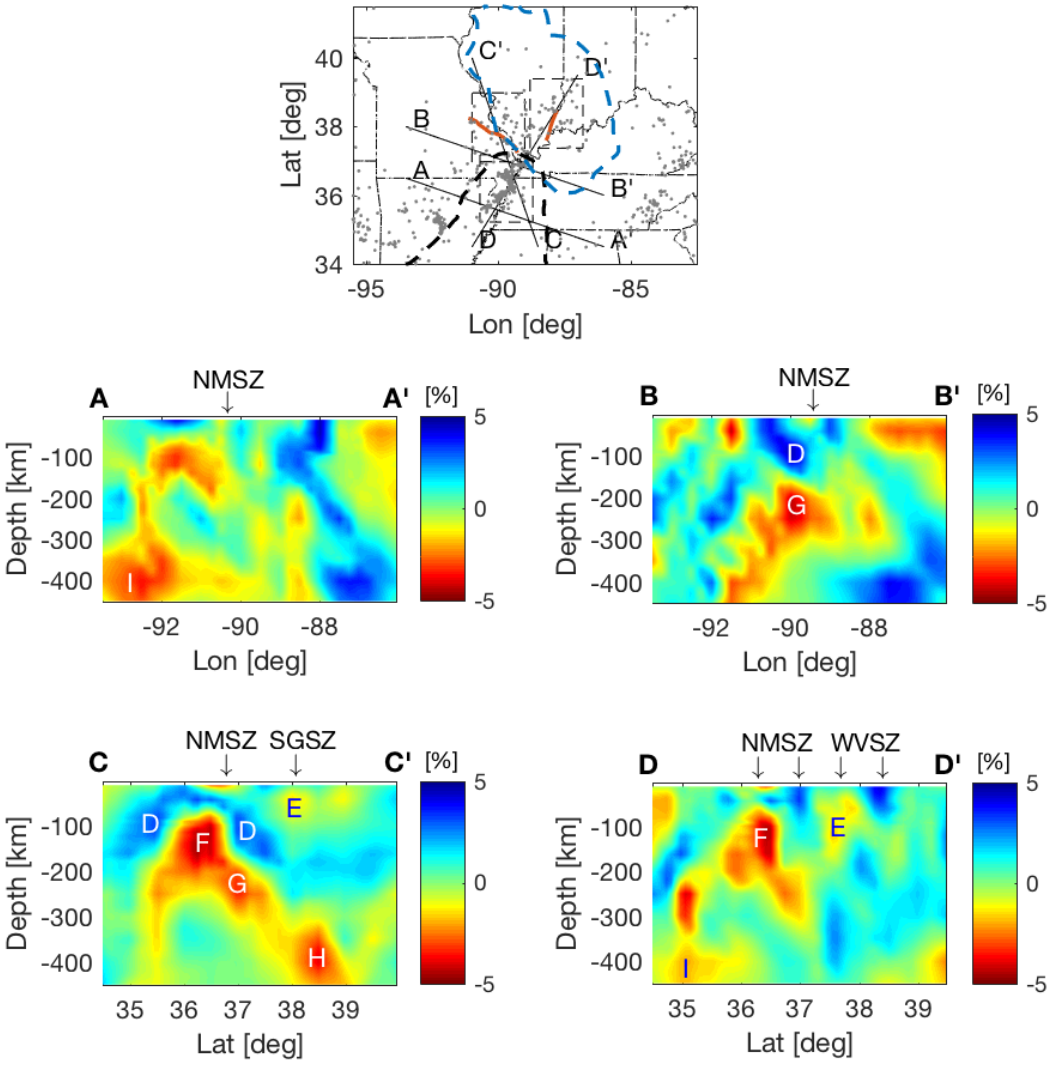

341

342 **Figure 11**. Vertical slices through the output Vs model. Vs and Vp anomalies have a similar

343 spatial distribution but, in most cases, the Vs anomalies have larger magnitudes.

344

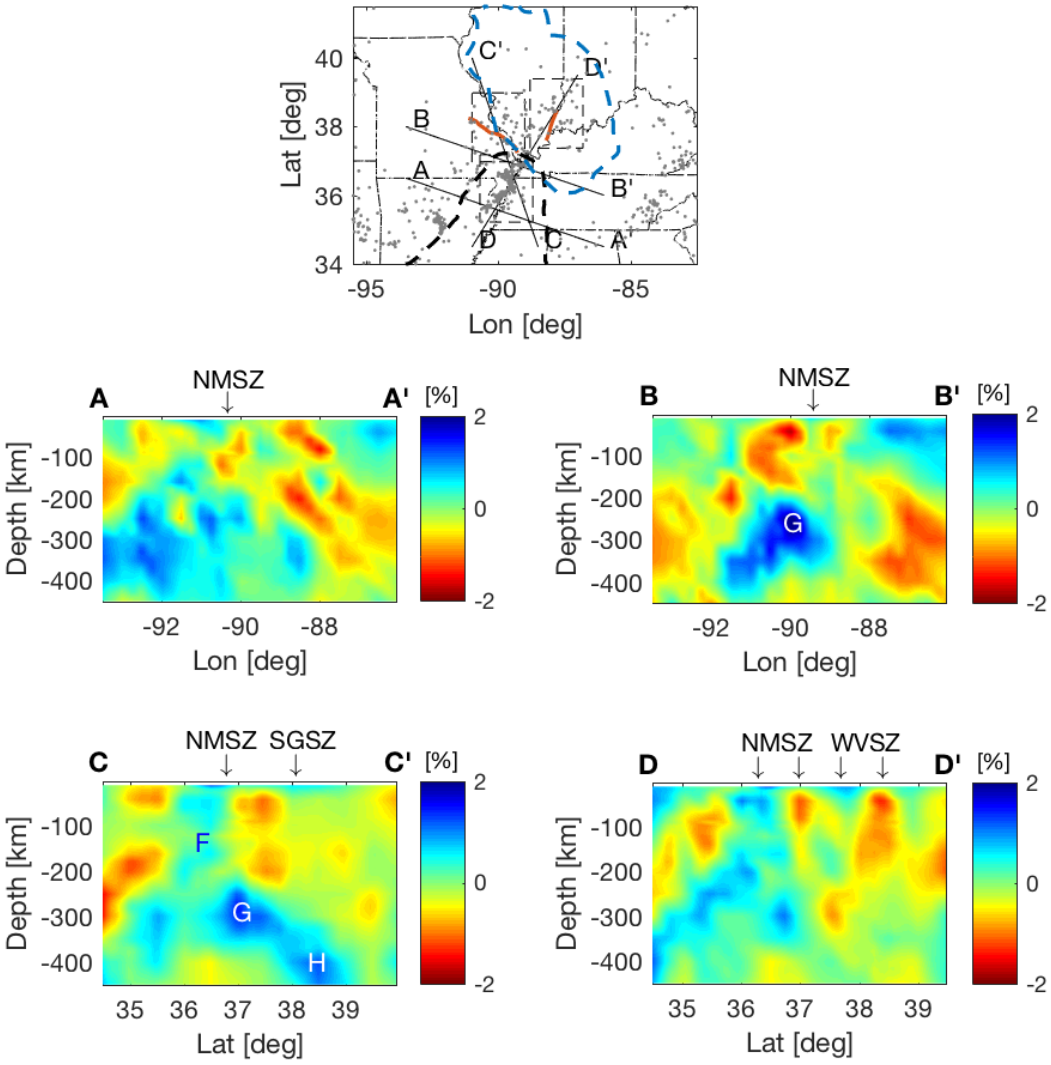

345

346 **Figure 12**. Vertical slices through the Vp /Vs ratio solution given as perturbation ratios with
347 respect to the initial model. Intraplate seismic zones are labeled as in Figure 11. Low Vp /Vs
348 ratios characterize low velocity anomalies G and H. No Vp /Vs variation is observed in the low-
349 velocity zone beneath the NMSZ in the upper mantle.

350

5 Interpretation

5.1 Crustal velocity structure

Anomalously high velocities in the lower crust characterize the upper Reelfoot Rift region and high velocities extend into the lowermost part of the Illinois Basin in the Vs solution. (labeled D in Figures 8–11). The spatial distribution of high crustal velocities resembles the patterns of anomalies resolved using ambient noise tomography (Liang and Langston, 2009) and shear velocity inversion (Chen et al., 2016). The pattern of high velocity at 40 km depth is also very similar to the location of uppermost mantle high velocity determined in a recent Pn velocity inversion (Basu and Powell, 2019). A linear, high-velocity anomaly (labeled A) is present in the crust beneath the central area of the Illinois Basin and coincides with the La Salle deformation belt. High velocity also extends in an EW direction across the northern Illinois basin. Prominent low velocity anomalies (labeled B in Figures 8 and 9) in southern Missouri coincide with a Bouguer gravity low interpreted as a batholith (the Missouri batholith of Hildenbrand and Hendricks, 1995). A prominent low velocity anomaly on the Arkansas-Oklahoma border (labeled C in Figures 8 and 9) corresponds to the Arkoma basin. Low velocity characterizes the lower crust below Kentucky and central and eastern Tennessee. This large low velocity region is also present in the Vs model determined by Chen et al. (2016).

5.2 Mantle velocity structure

Several interesting features are found in the mantle portions of the models. At 80 km depth, low velocity is present below the Reelfoot Rift and the Rough Creek graben. As indicated in cross sections CC’ and DD’, small regions of low velocity (labeled E in Figures 10 and 11) are present below the SGSZ and the WVSZ. These low velocity regions were also imaged in the Vs

model determined by Chen et al. (2016) at depths shallower than 75 km and may be better resolved equivalents of the more extensive low velocity region below the Illinois basin detected by Bedle and van der Lee (2006) using a limited number of stations.

The presence of prominent low-velocity anomaly F in cross sections CC' and DD' is consistent with the results of previous studies that identified reduced velocities in the mantle below the Reelfoot Rift and the Mississippi Embayment (e.g. Bedle and van der Lee, 2006; Pollitz and Mooney, 2014; Chen et al., 2016; Nyamwandha et al., 2016). Anomaly F extends to the SW at about a 45° angle below the Embayment in cross section DD', in agreement with the velocity models determined by Nyamwandha et al. (2016). An interesting new discovery is that low-velocity anomaly F also extends to the northwest at an apparent dip of ~45° along the boundary between Missouri and Illinois (anomaly G in cross section CC'). Anomaly G terminates at about 250 km depth but another, larger low velocity anomaly (H in cross section CC') continues along the same dip direction beginning at a depth of about 350 km. Anomaly H extends to the base of the model.

Low velocity is associated with the Mississippi Embayment mantle throughout the model. At a depth of about 350 km, the low velocity region broadens to the west (labeled I in Figures 8 and 9 and in cross section DD) and extends to the northeast below the Illinois basin (labeled H in Figures 8 and 9 and in cross section CC'). Low velocity region I is likely a continuation of the low-velocity anomaly that dips toward SW imaged below the Mississippi Embayment by Nyamwandha et al. (2016), considering that the orientation of anomaly I is the same as the dip direction of the low-velocity feature found in the earlier study. The depth slices at 350 and 400 km indicate the presence of a confined region of low velocity at the top of the transition zone and lends support to the interpretation by Nyamwandha et al. (2016) and Chen et

al. (2014) that the low velocities are associated with hot fluids upwelling from the transition zone.

The Vp/Vs model is presented in perturbation ratios with respect to the starting Vp/Vs model (Figure 12). On cross-section CC' of the Vp/Vs model, positive anomalies are associated with anomalies G and H, while no Vp/Vs anomaly is associated with anomaly F. In both our study and the study by Nyamwandha et al. (2016), the magnitudes of the Vp and Vs anomalies for anomaly F are very similar, leading to near zero Vp/Vs perturbations. In our study, Vs anomaly magnitude is higher than the associated Vp anomaly magnitude for G and H, producing positive Vp/Vs perturbations. This implies that the source of anomaly F may be different from that of anomalies G and H.

5.3 Synthetic tests

Synthetic models are constructed for anomalies F, G and H to investigate whether these anomalies form one continuous low velocity region or separate regions. The Vp and Vs input models are shown in Figures 13c and 13d, respectively. Synthetic arrival times are computed for all hypocenter-station pairs in the dataset used for the real tomographic inversion. The arrival times are randomly perturbed according to real data uncertainty and then inverted for recovered models using the same technique as the checkerboard resolution test described previously. Anomalous blocks F and G are separated by ~ 140 km (measured from the centers of the blocks) to represent two different regions in the initial model. The block edges are separated by ~40 km. Smearing in the recovered models connects the two blocks but does not reproduce the anomaly amplitude between the two blocks observed in the real solutions (Figures 13a and b). This suggests that anomalies F and G form a continuous region of low velocity in the real velocity models. Anomalies G and H are clearly separated from one another in the recovered synthetic

model for Vp. The result for Vs is less obvious but suggests that the weak Vs anomaly connecting G and H in the real solution may not be due to smearing; G and H could be a continuous region of low Vs. Continuity of the low Vs region is illustrated in the 3D view generated for the real data shown in Figure 14.

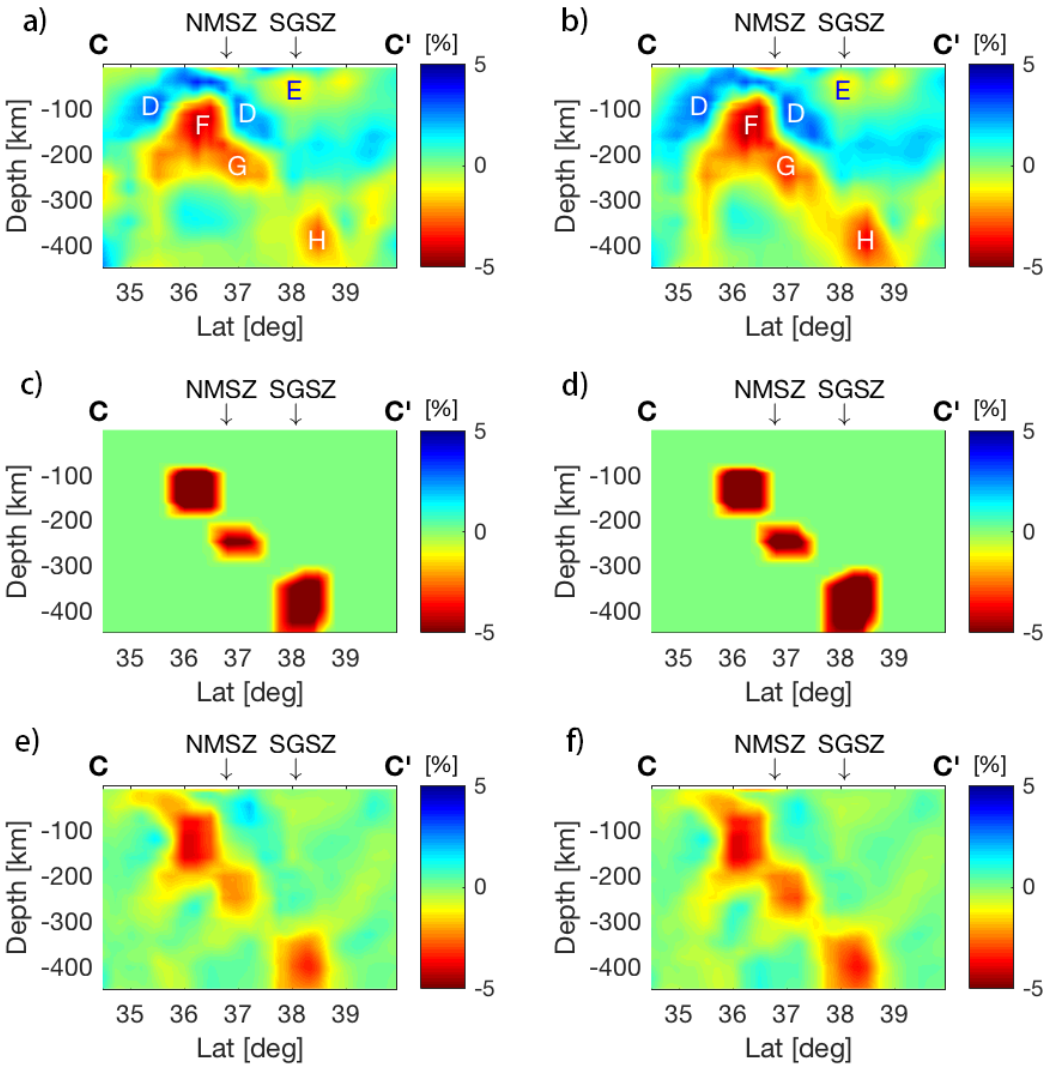

424 **Figure 13**. A synthetic test investigating the effect of artifacts on the resultant tomographic
425 images: (a) cross-section CC' of the Vp tomographic model; (b) cross-section CC' of the Vs
426 tomographic model; (c) cross section view of the input Vp synthetic model; (d) cross-section
427 view of the Vs synthetic input model; (e) recovered Vp model in the synthetic test; (f) recovered
428 Vs model in the synthetic test.

429

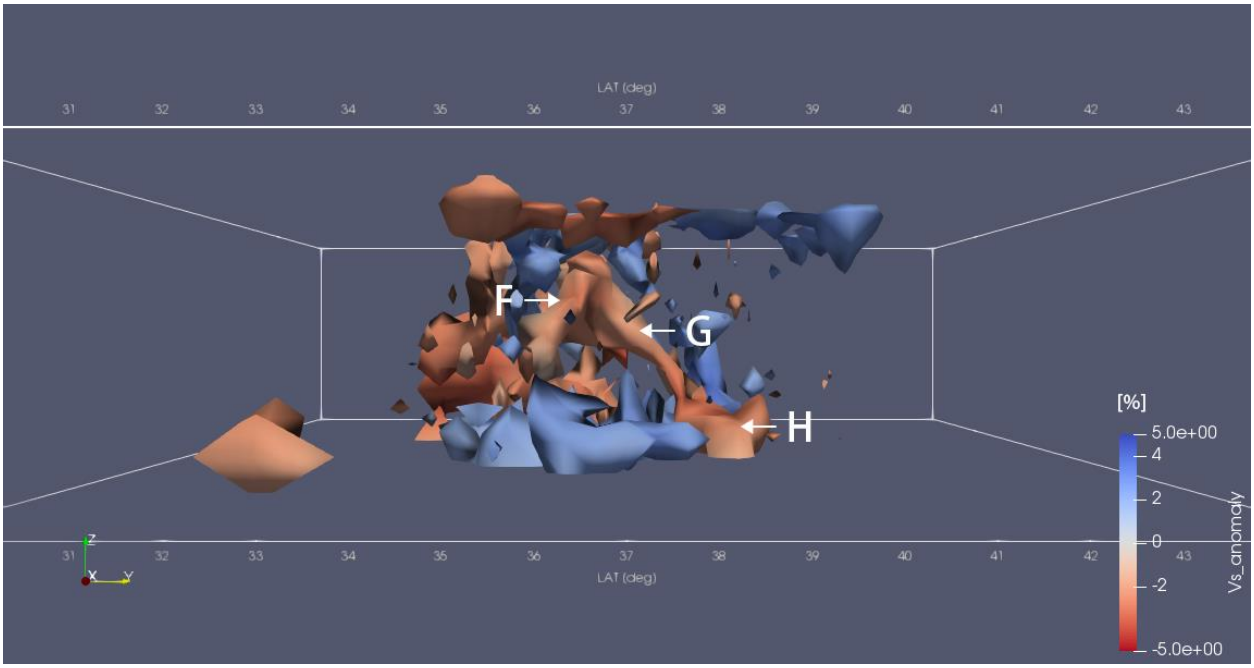

430

431 **Figure 14**. Three-dimensional view of the real Vs solution from the east. From this perspective,
432 the low Vs region (anomalies G and H) extends as a continuous feature from about 50 km depth
433 to the transition zone. The merger of the low velocity regions below the Illinois Basin and the
434 Mississippi Embayment is also visible.

435

6 Discussion

Our velocity models display some features that agree and some that disagree with previous velocity models for the crust, most notably the Vs model developed by Chen et al. (2016). The Chen et al. (2016) model was derived using surface waves recorded by TA and OIINK stations and covers most of the area investigated in our study. Velocity features in the crust that are in common to both studies include the presence of high velocity in the mid to lower crust below the Reelfoot Rift and southernmost Illinois Basin, and low velocity below Kentucky and parts of Tennessee. The two studies differ in the velocity associated with the La Salle fold belt; in the Chen et al. (2016) model, the fold belt is associated with low Vs while high Vs is found in our study. The presence of high velocity at mid to lower crustal depths would tend to support a rift origin for the deformational belt as rifting usually produces zones of high crustal velocity (Mooney et al., 1983). Marshak and Paulsen (1996) suggest that the La Salle belt formed as a result of extensional tectonism during formation of the Granite-Rhyolite province. The rift could have been subjected to compressional tectonics during the Appalachian Ouachtia orogeny, producing the complex anticlinal structure (McBride, 1997). Another possibility is that the high velocity rocks were emplaced during an episode of magmatic underplating associated with the formation of the Granite-Rhyolite province (Yang et al., 2017).

The origin of slow velocity lower crust throughout Kentucky and central and eastern Tennessee is enigmatic. The slow velocity region does not correlate with low Bouguer or isostatic gravity anomalies or with obvious terrane boundaries such as the Grenville front. Most of the region is underlain with thinned lithosphere attributed to lithospheric foundering in the teleseismic Vp study by Biryol et al. (2016). Possibly, the proposed foundering event caused heating and chemical differentiation in the lower crust, resulting in the generation of low

459 velocity, silica rich magmas, as hot asthenosphere replaced normal cool lithosphere. The upper
460 crust was not affected as age dating indicates the presence of Granite-Rhyolite as far east as
461 central Kentucky and Tennessee (Fisher, 2010).

462 Our velocity models reveal the presence of low-velocity anomalies at depths exceeding
463 150 km beneath the central part of the Illinois Basin. Anomalies G and H form a northwest
464 dipping low velocity zone that is a northern extension of the well documented LVZ below the
465 Mississippi Embayment (anomaly F). The northwest dipping LVZ extends from roughly 200 km
466 to the transition zone. Our synthetic tests indicate that anomaly G is probably continuous with
467 anomaly F. Anomaly H is an isolated feature in the Vp model but the larger Vs anomalies
468 suggest that the feature is continuous with anomaly G in the Vs model. In the study by
469 Nyamwandha et al. (2016), anomaly F is most evident at depths of 100 ~ 200 km where it is
470 approximately 100 km wide. Regions of high velocity are imaged at depths of 80 ~ 160 km
471 along the sides and above the low-velocity anomaly. The high velocity regions are also found in
472 our study and are labeled D in cross-sections BB' and CC' (Figures 10 and 11).

473 The presence of a dipping low velocity zone in the upper mantle bounded over part of its
474 length by regions with high Vp and Vs anomalies is strikingly similar to upper mantle velocity
475 models determined for the North China Craton. The velocity anomalies below China are
476 attributed to upwelling, silica-rich fluids from the stalled Pacific slab (e.g. Santosh et al., 2010).
477 Nyamwandha et al. (2016) suggest that hot, hydrous, upwelling fluids from the stalled Laramide
478 slab in the transition zone (Sigloch et al., 2008; Sigloch, 2011) produce the low Vp and Vs
479 anomalies below the Mississippi Embayment (anomaly F). Observed high-velocity regions
480 above and flanking the low-velocity region are interpreted as depleted, lowermost lithosphere, in
481 agreement with the interpretation of similar high-velocity regions below the North China Craton

(Santosh et al., 2010; Tian and Zhao, 2011). The results of our study, indicating that the LVZ below the ME extends to the transition zone, supports the interpretation by Nyamwandha et al. (2016).

The new discovery of a second LVZ (anomalies G and H) extending to the transition zone below the Illinois Basin supports the concept that rising, hot fluids are critical factors in the generation of the velocity anomalies. Seismic velocities in the mantle are mainly affected by three factors: temperature variations, the existence of fluids, and compositional changes. In general, Vp and Vs anomaly magnitudes are dissimilar because Vs is more sensitive to changes in these factors than Vp (Schmandt and Lin, 2014). This is the case for anomalies G and H in our model. Anomaly F is unusual in that the Vp and Vs magnitudes are very similar. We investigate the relative importance of the factors that affect velocity for anomalies G and H at the midpoint of each anomaly, 240 km for G and 370 km for H. Maximum Vp and Vs anomalies are -4% and -5%, respectively, at 240 km and -3.8% and -5%, respectively, at 370 km.

6.1 The influence of temperature

Mantle rheology can be significantly affected by temperature. Cammarano et al. (2003) demonstrated that the sensitivity of velocity to temperature decreases with increasing depth. We derive the equations for estimating temperature elevations from the observed low velocity anomalies G and H at 240 km and 370 km, as presented in supporting information **Text S3**. Our calculations show that temperature increases of 830±150° and 470 ± 120° are required to produce the Vp and Vs anomalies at location G, respectively; and temperature increases of 740 ± 140° and 550 ± 120° are required to produce the Vp and Vs anomalies at location H, respectively. Temperature increases by these amounts are too high for mantle materials to remain solid (Hammond and Humphreys, 2000) as can be determined by comparing the geotherm with the

505 solidus at 240 km and 370 km depths. The magnitudes of our observed Vp and Vs anomalies do
506 not support the presence of extensive melting. Some other factors must be taken into
507 consideration to help explain the reduced mantle velocities in our models.

508 6.2 Compositional changes

509 Many calculations in previous seismic tomographic studies based on experimentally
510 derived temperature derivatives of seismic velocities tend to require unrealistically large thermal
511 anomalies (e.g. Frederiksen et al., 1998). Our case is not an exception. The overly large
512 temperature variations suggest that other sources of velocity reduction that produce changes in
513 mantle rocks over long time periods, such as mineral reactions, should be taken into
514 consideration (e.g. Sobolev and Babeyko, 1994).

515 Several studies address the sensitivity of seismic velocities to composition (e.g. Lee,
516 2003; Schutt and Lesher, 2006; Wagner et al., 2008). Lee [2003] investigated the effects of
517 mantle compositional variations on density and seismic velocities for a suite of upper mantle
518 peridotites spanning the primary compositional range of fertile (magnesium number: Mg# = 100
519 × Mg/(Mg + Fe) of 86–88) to highly residual compositions (Mg# of 93–94). Using the method
520 in Lee (2003), our calculation indicates that the maximum Vs anomalies that can be produced
521 from the reduction of magnesium number are −2.3% ~ −2.7% for anomaly G and −2.2% ~
522 −2.5% for anomaly H. However, Vp is relatively insensitive to the variation of magnesium
523 number (Lee, 2003). Therefore, the velocity reductions in the mantle beneath the Illinois Basin
524 cannot be explained by the variation of Mg# alone. Details of the calculation are presented in
525 supporting information **Text S4**.

We consider the possibility that the velocity anomalies could be due to changes in rock type only. We calculate Vp and Vs anomalies with respect to hartzburgite for various rock types that may be expected in the upper mantle using the Burman mineral physics toolbox (Cottaar et al., 2014). The result indicates that purely compositional changes cannot account for the observed Vp and Vs anomaly values. In addition, invoking a sudden compositional change in a localized region to explain the velocity anomalies is improbable. Details of the calculation are presented in supporting information **Text S5**. Our calculation utilizes the data from Duffy and Anderson (1989), McDonough and Rudnick (1998), Lowrie (2007), van der Lee et al. (2008), and Irifune et al. (2008).

6.3 Water enrichment

Water enrichment in the mantle can reduce both Vp and Vs (Jacobsen et al., 2004; Bastow et al., 2008; Eaton et al., 2009; Mao et al., 2011). Water reduces mantle velocities by saturating minerals such as olivine, resulting in increased anelasticity and attenuation (Dixon et al., 2004). Water can also reduce Vp and Vs by metasomatic alteration of mantle peridotite or eclogite (Sobolev and Babeyko, 1994; Goes and van der Lee, 2002; Mainprice et al., 2008; Pollitz and Mooney, 2014). Elevated water levels could be the result of rising, hydrated asthenosphere at hotspot locations (Pollitz and Mooney, 2014) and dehydration of descending slabs (Dixon et al., 2004; Santosh et al., 2010; Chen et al., 2014; Nyamwandha et al., 2016).

We calculated Vp and Vs reductions that would result from water contents of 900 ppm and 1500 ppm H/Si in olivine for depths of 240 and 370 km, respectively, following the procedures in Karato (2003) and using the data provided by Minster and Anderson (1981), Anderson and Given (1982), Goes et al. (2000), Dixon et al. (2004), and Dalton et al. (2008) (see supporting information **Text S6** for details). With these solubilities, the Vp reductions are ~

549 1.2% and ~ 1.6% at 240 and 370 km, respectively and the Vs reductions are ~ 1.9% and ~ 2.5%
550 at 240 km and 370 km, respectively. These reductions account for about one-third of the
551 observed anomaly at 240 km, and less than half of the anomaly at 370 km. We note that
552 introducing water into pyroxene and garnet would further reduce upper mantle shear velocities
553 (Smith et al., 1999; Grant et al., 2007; Yang et al., 2008).

554 6.4 Other factors

555 Our calculations so far for Vp and Vs reduction due to increased water content and
556 compositional variations are summarized in Table 1. To account for the observed anomalies,
557 additional velocity reductions of $\Delta Vp = -269$ m/s and $\Delta Vs = -22 \sim -37$ m/s are required at 240
558 km and $\Delta Vp = -189$ m/s and $\Delta Vs = 0 \sim -13$ m/s are needed at 370 km. As discussed above,
559 these additional velocity reductions could be attributed to temperature variations. However,
560 temperature variations alone cannot account for the differences in the additional velocity
561 reductions because the magnitude of ΔVp is about ten times higher than the magnitude of ΔVs.
562 Some other factors, in addition to temperature elevation, should be considered to help explain the
563 reduced Vp.

564 Schutt and Lesher (2010) investigated the effects of several dominant compositional
565 trends on velocity and density and showed that at cratonic mantle (< 200 km) temperatures and
566 pressures, orthopyroxene (opx) enrichment results in little change in Vs but decreases Vp and the
567 Vp/Vs ratio. Another conclusion drawn by Schutt and Lesher (2010) is that melt depletion has
568 little effect on Vp but leads to increased Vs and decreased Vp/Vs ratio. The signs and
569 magnitudes of the ΔVp and ΔVs required to satisfy our observations are not compatible with
570 melt depletion but suggest that a missing factor that is needed to explain the reduced Vp might
571 be an increase of the opx volume fraction.

572 We investigate the possibility of opx enrichment using a simple approach. Assuming
573 mantle rocks consist of opx and olivine, simultaneous inversion for ΔVp and ΔVs using the
574 sensitivities of seismic velocities to opx (Schutt and Lesher, 2010) and to elastic moduli
575 (Cammarano et al., 2003) indicates that a temperature elevation of 170 ± 10°C and an opx
576 volume fraction of ~ 60% are needed to produce the ΔVp and ΔVs values at 240 km. Similarly, a
577 temperature elevation of 100 ± 10°C and an opx volume fraction of ~ 50% are needed to produce
578 the ΔVp and ΔVs values at 370 km. Temperature elevations of these magnitudes would not result
579 in melt. A detailed description of the inversion is given in Saxena (2020).

580 The magnitudes of the inverted opx contents computed above are higher than those
581 determined in previous studies on opx enrichment. The maximum opx content found by Wagner
582 et al. (2008) for the Kaapvaal southern Africa craton is 45%. Li et al. (2008) find a maximum
583 opx content of 40% for the Colorado Plateau. Cratonic xenolith suits from Kaapvaal and
584 Udachnaya, Siberia, range between 20 and 50% modal opx (Bernstein et al., 2007). Our results
585 are not entirely unreasonable, and we suggest that opx enrichment is probably a factor in the
586 reduction of Vp relative to Vs. Smaller amounts of opx might be required by modifying the
587 assumptions made in our calculations of the effects of Mg#, compositional variations and water
588 content. Possible sources of error in our calculations are discussed in supporting information
589 **Text S7**.

590 6.5 Tectonic implications

591 Our analysis of the possible factors that are producing the observed LVZ below the
592 Illinois basin is compatible with the results for the LVZ below the ME; in both cases, opx
593 enrichment can account for the large magnitude, negative Vp anomalies (Nyamwandha et al.,
594 2016; Saxena et al., 2017; Saxena, 2020). A likely source for the opx enrichment is

595 metasomatism of olivine-rich mantle rocks by silica rich fluids ascending from flat slab remnants
596 trapped in the transition zone. The most likely source for silica in a slab remnant is subducted
597 ocean crust and sediment. Silica is transported into the overlying mantle during slab dehydration
598 and subsequent water-rock reactions (Kelemen et al., 1998; Wagner et al., 2008). Much of the
599 released water is concentrated in and above the mantle transition zone and rising hydrated fluids
600 produce metasomatic reactions in the overlying mantle (Niu, 2005; Kusky et al., 2007; Windley
601 et al., 2010; Pollitz and Mooney, 2014), eventually converting olivine into opx (Bell et al., 2005).

602 The likelihood that hydrous phases will survive to transition zone depths increases if the
603 slab is old (>50 Ma), subducts at a high rate and contains thick ocean crust (e.g. Kusky et al.,
604 2014; Maruyama and Okamoto, 2007). These conditions were met for the Farallon slab during
605 the late Cretaceous Laramide orogeny with the arrival of the buoyant Hess and Shatsky oceanic
606 plateaus. Subduction of the plateaus is regarded as a primary factor in the flattening of the
607 Farallon slab (e.g. Liu and Currie, 2016). Liu et al. (2008; 2010) developed a reverse convection
608 model for the locations of the plateaus over time. The reconstructed location of the Hess plateau
609 places the top just below the transition zone in the central US, coincident with the prominent
610 LVZ at 400 km depth in our model. We suggest that the LVZ is directly related to the presence
611 of the Hess plateau.

612 A question arises as to why the LVZ would be so prominent below the Mississippi
613 Embayment and the Illinois Basin and not in other locations that also passed over the Hess
614 plateau. The answer lies in the tectonic history of the region. We suggest that the lithosphere
615 below the Mississippi Embayment and the Illinois Basin is thinned by prior tectonic activity and
616 forms a natural conduit for the ascension of hot, hydrated fluids from the trapped plateau (e.g.
617 Burov et al., 2007). The Reelfoot Rift and Rough Creek graben are part of a late stage

618 intracratonic fault system associated with the breakup of supercontinent Rodinia (e.g. Thomas,
619 2006; 2014). Rifted crust probably extends below the entire ME (Johnson et al, 1994; Cox and
620 van Arsdale, 1997; 2002). Although crustal extension was not extensive, the rifting probably
621 thinned the lithosphere and may have introduced fertile mantle material. The origin of the Illinois
622 Basin remains enigmatic but there is mounting evidence that the southern portion of the basin
623 was affected by the same rifting episode that produced the Reelfoot Rift (e.g. Chen et al., 2016).
624 Our velocity models support the possibility that the crust was rifted along the La Salle fold belt
625 prior to development of the basin.

626 In addition to rifting, the passage of hotspots played an important role in thinning the
627 lithosphere. The Mississippi Embayment was affected by passage of the Bermuda hotspot in mid
628 Cretaceous time as evidenced by the intrusion of a suite of ultramafic and alkali rocks along and
629 within the Reelfoot Rift; the suite of intrusions suggests widespread, thermal modification of the
630 mantle below the embayment (Cox and van Arsdale, 1997; 2002). The Illinois Basin may have
631 passed over another hotspot in the Cretaceous. Chu et al. (2013) suggest that a hotspot affected
632 the southern and central part of the basin (Figure 1) based on variations in the amplitudes of
633 regional seismic waveforms. Associated geodynamic modeling to determine the predicted
634 seismic signal of an evolving hotspot indicated substantial thinning of the lithosphere. The path
635 of the hotspot crosses the basin in a WNW direction and passes over the location of anomaly H
636 in our velocity models.

637 6.6 Implications for the origin of intraplate seismicity

638 Considerable effort has been made to understand the effect of the low velocity zone
639 below the Reelfoot Rift (anomaly F) on the generation of earthquakes in the NMSZ. Pollitz and
640 Mooney (2014) hypothesized that the low-velocity mantle volume is weaker than its

surroundings, and consequently, the Reelfoot Rift has relatively low elastic plate thickness. As a result, tectonic stress would tend to concentrate within this zone (Kenner and Segall, 2000). Chen et al. (2014) and Nyamwandha et al. (2016) interpreted the low velocities as a viscously weak zone with low shear strength embedded in the stronger lithosphere. Tectonic stress will concentrate in the weak zone and transfer to seismogenic faults in the upper crust. This hypothesis is supported by geodynamic modeling (Zhan et al., 2016). The presence of low velocity anomaly E (Figures 10 and 11) in our study is located below the SGSZ and may play an important role in stress concentration in the SGSZ. Similarly, the presence of low velocity anomaly E below the WVSZ (profile CC' in Figures 10 and 11) may be responsible for elevated stress in this location. As is also suggested by Chen et al. (2016), additional numerical modeling is needed to access the impact of the low velocity regions on earthquake generation.

7 Conclusions

Detailed Vp and Vs models are developed for the upper mantle below the northern Missisippi Embayment and Illinois Basin. Good resolution is obtained to a depth of 400 km. We image the LVZ below the embayment found in several previous studies and best resolved in the joint Vp and Vs inversion by Nyamwandha et al. (2016). Our results extend the low velocity zone determined by Nyamwandha et al. (2016) to transition zone depths, supporting the conclusion that the low velocities are produced by hydrous fluids ascending from a trapped portion of the Farallon slab. We detect another LVZ dipping to the northwest below the Illinois Basin. This LVZ consists of two segments; the upper segment is present in the depth range 200 to 300 km and appears to be an extension of the LVZ below the Mississippi Embayment. The second segment is offset to the northwest and extends from ~ 300 km to the transition zone. We calculate the possible contributions of elevated temperature, compositional variations and

elevated fluid content to explain the presence of the LVZ and conclude that a reasonable contribution from all three cannot explain the low Vp anomalies without the presence of elevated orthopyroxene concentrations. This result adds additional support to the conclusion that the LVZs below the Mississippi Embayment and the Illinois Basin are linked to the presence of a slab fragment located below the region. We suggest that the fragment is the portion of the Farallon slab that contains the Hess plateau.

Acknowledgment

We would like to thank Cecilia Nyamwandha for providing the arrival time data used in her Ph.D. dissertation. We thank Xiaoting Lou from the Northwestern University for developing the Python/Matplotlib tool used in this study for measuring teleseismic arrival times. Dr. Hersh Gilbert from the Purdue University kindly provided the crustal thickness dataset for the central United States built upon a receiver function analysis. We obtained seismic event data from the IRIS Data Management Center (DMC) (http://ds.iris.edu/ds/nodes/dmc/) through a computer software called JWEED. Support was provided by the Center for Earthquake Research and Information at the University of Memphis.

Table 1. Velocity anomalies observed at 240 km and 370 km and the anomalies produced by elevated water and compositional variations. Anomalies required from other factors (ΔVp and ΔVs) are calculated by subtracting the contributions of water and changing magnesium number from the total anomalies.

		Total	Water	Mg#	Remainder
Anomaly G	ΔVp [m/s]	−372	−103	0	−269
(240 km)	ΔVs [m/s]	−229	−85	−107 ~ −122	−22 ~ −37
Anomaly H	ΔVp [m/s]	−336	−147	0	−189
(370 km)	ΔVs [m/s]	−240	−120	−107 ~ −122	0 ~ −13

References

Anderson, D. L. & Given, J. W. (1982). Absorption band q model for the earth. *Journal of Geophysical Research: Solid Earth*, 87(B5):3893–3904.

Bastow, I., Nyblade, A., Stuart, G., Rooney, T., & Benoit, M. (2008). Upper mantle seismic structure beneath the ethiopian hot spot: Rifting at the edge of the african low-velocity anomaly. *Geochemistry, Geophysics, Geosystems*, 9(12).

Basu, U. & Powell, C. (2019). Pn tomography and anisotropy study of the central united states. *Journal of Geophysical Research: Solid Earth*, 124(7):7105–7119.

Bedle, H. & van der Lee, S. (2006). Fossil flat-slab subduction beneath the illinois basin, usa. *Tectonophysics*, 424(1-2):53–68.

Bell, D. R., Gregoire, M., Grove, T., Chatterjee, N., Carlson, R., & Buseck, P. (2005). Silica and volatile-element metasomatism of archean mantle: a xenolith-scale example from the kaapvaal craton. *Contributions to Mineralogy and Petrology*, 150(3):251.

Bernstein, S., Kelemen, P. B., & Hanghøj, K. (2007). Consistent olivine Mg# in cratonic mantle reflects Archean mantle melting to the exhaustion of orthopyroxene. *Geology, 35*(5), 459-462.

Bickford, M., Van Schmus, W., Karlstrom, K., Mueller, P., & Kamenov, G. (2015). Mesoproterozoic-trans-laurentian magmatism: A synthesis of continent-wide age distributions, new sims u–pb ages, zircon saturation temperatures, and hf and nd isotopic compositions. *Precambrian Research*, 265:286–312.

Braile, L. W., Hinze, W. J., Keller, G. R., Lidiak, E. G., & Sexton, J. L. (1986). Tectonic development of the new madrid rift complex, mississippi embayment, north america. *Tectonophysics*, 131(1-2):1–21.

Burov, E., Guillou-Frottier, L., d'Acremont, E., Le Pourhiet, L., & Cloetingh, S. A. P. L. (2007). Plume head–lithosphere interactions near intra-continental plate boundaries. *Tectonophysics*, *434*(1-4), 15-38.

Cammarano, F., Goes, S., Vacher, P., & Giardini, D. (2003). Inferring upper-mantle temperatures from seismic velocities. *Physics of the Earth and Planetary Interiors*, 138(3- 4):197–222.

Carter, N. L. & Ave'Lallemant, H. G. (1970). High temperature flow of dunite and peridotite. *Geological Society of America Bulletin*, 81(8):2181–2202.

722 Catchings, R. (1999). Regional Vp, Vs, Vp/Vs, and poisson's ratios across earthquake source
723 zones from memphis, tennessee, to st. louis, missouri. *Bulletin of the Seismological*
724 *Society of America*, 89(6):1591–1605.

725 Chen, C., Gilbert, H., Andronicos, C., Hamburger, M. W., Larson, T., Marshak, S., Pavlis, G. L.,
726 & Yang, X. (2016). Shear velocity structure beneath the central united states:
727 implications for the origin of the illinois basin and intraplate seismicity. *Geochemistry,*
728 *Geophysics, Geosystems*, 17(3):1020–1041.

729 Chen, C., Zhao, D., & Wu, S. (2014). Crust and upper mantle structure of the new madrid
730 seismic zone: Insight into intraplate earthquakes. *Physics of the Earth and Planetary*
731 *Interiors*, 230:1–14.

732 Chopra, P., Paterson, & MS (1981). The experimental deformation of dunite. *Tectonophysics*,
733 78(1-4):453–473.

734 Chu, R., Leng, W., Helmberger, D. V., & Gurnis, M. (2013). Hidden hotspot track beneath the
735 eastern United States. *Nature Geoscience, 6*(11), 963-966.

736 Cottaar, S., Heister, T., Rose, I., & Unterborn, C. (2014). Burnman: A lower mantle mineral
737 physics toolkit. *Geochemistry, Geophysics, Geosystems*, 15(4):1164–1179.

738 Cox, R. T., & Van Arsdale, R. B. (1997). Hotspot origin of the Mississippi embayment and its
739 possible impact on contemporary seismicity. *Engineering Geology, 46*(3-4), 201-216.

740 Cox, R. T. & Van Arsdale, R. B. (2002). The mississippi embayment, north america: A first
741 order continental structure generated by the cretaceous superplume mantle event. *Journal*
742 *of Geodynamics*, 34(2):163–176.

743 Csontos, R., Van Arsdale, R., Cox, R., & Waldron, B. (2008). Reelfoot rift and its impact on
744 quaternary deformation in the central mississippi river valley. *Geosphere*, 4(1):145–158.

745 Dalton, C. A., Ekstr¨om, G., & Dziewon´ski, A. M. (2008). The global attenuation structure of
746 the upper mantle. *Journal of Geophysical Research: Solid Earth*, 113(B9).

747 Demouchy, S., Tommasi, A., Barou, F., Mainprice, D., & Cordier, P. (2012). Deformation of
748 olivine in torsion under hydrous conditions. *Physics of the Earth and Planetary Interiors*,
749 202:56–70.

750 Dixon, J. E., Dixon, T. H., Bell, D., & Malservisi, R. (2004). Lateral variation in upper mantle
751 viscosity: role of water. *Earth and Planetary Science Letters*, 222(2):451–467.

752 Duffy, T. S. & Anderson, D. L. (1989). Seismic velocities in mantle minerals and the mineralogy
753 of the upper mantle. *Journal of Geophysical Research: Solid Earth*, 94(B2):1895–1912.

754 Eaton, D. W., Darbyshire, F., Evans, R. L., Gru¨tter, H., Jones, A. G., & Yuan, X. (2009). The
755 elusive lithosphere–asthenosphere boundary (lab) beneath cratons. *Lithos*, 109(1-2):1–
756 22.

757 Eaton, D. W. & Frederiksen, A. (2007). Seismic evidence for convection-driven motion of the
758 North American plate. *Nature*, 446(7134):428.

759 Eberhart-Phillips, D. (1986). Three-dimensional velocity structure in northern california coast
760 ranges from inversion of local earthquake arrival times. *Bulletin of the Seismological*
761 *Society of America*, 76(4):1025–1052.

762 Frederiksen, A., Bostock, M., VanDecar, J., & Cassidy, J. (1998). Seismic structure of the upper
763 mantle beneath the northern canadian cordillera from teleseismic travel-time inversion.
764 *Tectonophysics*, 294(1-2):43–55.

765 Gao, S. S. & Liu, K. H. (2014). Mantle transition zone discontinuities beneath the contiguous
766 united states. *Journal of Geophysical Research: Solid Earth*, 119(8):6452–6468.

767 Goes, S., Govers, R., Vacher, & P (2000). Shallow mantle temperatures under europe from p and
768 s wave tomography. *Journal of Geophysical Research: Solid Earth*, 105(B5):11153–
769 11169.

770 Goes, S. & van der Lee, S. (2002). Thermal structure of the north american uppermost mantle
771 inferred from seismic tomography. *Journal of Geophysical Research: Solid Earth*,
772 107(B3):ETG–2.

773 Grant, K., Ingrin, J., Lorand, J. P., & Dumas, P. (2007). Water partitioning between mantle
774 minerals from peridotite xenoliths. *Contributions to Mineralogy and Petrology*,
775 154(1):15–34.

776 Hammond, W. C. & Humphreys, E. D. (2000). Upper mantle seismic wave velocity: Effects of
777 realistic partial melt geometries. *Journal of Geophysical Research: Solid Earth*,
778 105(B5):10975–10986.

779 Heine, C., Mu¨ller, R. D., Steinberger, B., & Torsvik, T. H. (2008). Subsidence in
780 intracontinental basins due to dynamic topography. *Physics of the Earth and Planetary*
781 *Interiors*, 171(1-4):252–264.

782 Hildenbrand, T. G., & Hendricks, J. D. (1995). Geophysical setting of the Reelfoot rift and
783 relations between rift structures and the New Madrid seismic zone (No. 1538-E).

784 Jacobsen, S. D., Smyth, J. R., Spetzler, H., Holl, C. M., & Frost, D. J. (2004). Sound velocities
785 and elastic constants of iron-bearing hydrous ringwoodite. *Physics of the Earth and*
786 *Planetary Interiors*, 143:47–56.

787 Johnson, P. R., Zietz, I., & Thomas, W. A. (1994). Possible Neoproterozoic-early Paleozoic
788 grabens in Mississippi, Alabama, and Tennessee. *Geology*, *22*(1), 11-14.

789 Karato, S.-i. (2003). Mapping water content in upper mantle. *Geophysical Monograph-*
790 *American Geophysical Union*, 138:135–152.

791 Karato, S.-I., Paterson, M. S., & FitzGerald, J. D. (1986). Rheology of synthetic olivine
792 aggregates: influence of grain size and water. *Journal of Geophysical Research: Solid*
793 *Earth*, 91(B8):8151–8176.

794 Kawamoto, T. (2006). Hydrous phases and water transport in the subducting slab. *Reviews in*
795 *Mineralogy and Geochemistry*, 62(1):273–289.

796 Kelemen, P. B., Hart, S. R., & Bernstein, S. (1998). Silica enrichment in the continental upper
797 mantle via melt/rock reaction. *Earth and Planetary Science Letters*, *164*(1-2), 387-406.

798 Keller, G., Lidiak, E., Hinze, W., & Braile, L. (1983). The role of rifting in the tectonic
799 development of the midcontinent, usa. In *Developments in Geotectonics*, volume 19,
800 pages 391–412. Elsevier.

801 Kenner, S. J. & Segall, P. (2000). A mechanical model for intraplate earthquakes: Application to
802 the new madrid seismic zone. *Science*, 289(5488):2329–2332.

803 Kennett, B. & Engdahl, E. (1991). Traveltimes for global earthquake location and phase
804 identification. *Geophysical Journal International*, 105(2):429–465.

805 Kusky, T., Windley, B., & Zhai, M.-G. (2007). Tectonic evolution of the north china block: from
806 orogen to craton to orogen. *Geological Society, London, Special Publications*, *280*(1):1–
807 34.

Kusky, T. M., Windley, B. F., Wang, L., Wang, Z., Li, X., & Zhu, P. (2014). Flat slab subduction, trench suction, and craton destruction: comparison of the north china, wyoming, and brazilian cratons. *Tectonophysics*, 630:208–221.

Laske, G., Masters, G., Ma, Z., & Pasyanos, M. (2013). Update on crust1. 0—a 1-degree global model of earth's crust. In *Geophys. Res. Abstr*, volume 15, page 2658. EGU General Assembly Vienna, Austria.

Lee, C.-T. A. (2003). Compositional variation of density and seismic velocities in natural peridotites at stp conditions: Implications for seismic imaging of compositional heterogeneities in the upper mantle. *Journal of Geophysical Research: Solid Earth*, 108(B9).

Li, Q., Liu, M., & Sandvol, E. (2005). Stress evolution following the 1811–1812 large earthquakes in the new madrid seismic zone. *Geophysical Research Letters*, 32(11).

Li, Q., Liu, M., Zhang, Q., & Sandvol, E. (2007). Stress evolution and seismicity in the central-eastern united states: Insights from geodynamic modeling. *Special Papers-Geological Society of America*, 425:149.

Liang, C. & Langston, C. A. (2009). Three-dimensional crustal structure of eastern north america extracted from ambient noise. *Journal of Geophysical Research: Solid Earth*, 114(B3).

Liu, S., & Currie, C.A. (2016). Farallon plate dynamics prior to the Laramide orogeny: numerical models of flat subduction, *Tectonophysics*, 666, p.33-47, doi 10.1016/j.tecto.2015.10.010.

Liu, L., Gurnis, M., Seton, M., Saleeby, J., Mu¨ller, R. D., & Jackson, J. M. (2010). The role of oceanic plateau subduction in the laramide orogeny. *Nature Geoscience*, 3(5):353.

Lou, X., van der Lee, S., & Lloyd, S. (2013). Aimbat: A python/matplotlib tool for measuring teleseismic arrival times. *Seismological Research Letters*, 84(1):85–93.

Mackwell, S., Kohlstedt, D., & Paterson, M. (1985). The role of water in the deformation of olivine single crystals. *Journal of Geophysical Research: Solid Earth*, 90(B13):11319–11333.

Mainprice, D., Le Page, Y., Rodgers, J., & Jouanna, P. (2008). Ab initio elastic properties of talc from 0 to 12 gpa: interpretation of seismic velocities at mantle pressures and prediction of auxetic behaviour at low pressure. *Earth and Planetary Science Letters*, 274(3-4):327–338.

Mao, Z., Jacobsen, S. D., Frost, D. J., McCammon, C. A., Hauri, E. H., & Duffy, T. S. (2011). Effect of hydration on the single-crystal elasticity of fe-bearing wadsleyite to 12 gpa. *American Mineralogist*, 96(10):1606–1612.

Marshak, S. & Paulsen, T. (1996). Midcontinent us fault and fold zones: A legacy of proterozoic intracratonic extensional tectonism? *Geology*, 24(2):151–154.

Maruyama, S. & Okamoto, K. (2007). Water transportation from the subducting slab into the mantle transition zone. *Gondwana Research*, 11(1-2):148–165.

McBride, J. H. (1997). Variable deep structure of a midcontinent fault and fold zone from seismic reflection: La salle deformation belt, Illinois basin. *Geological Society of America Bulletin*, 109(11):1502–1513.

McBride, J. H., Kolata, D. R., & Hildenbrand, T. G. (2003). Geophysical constraints on understanding the origin of the illinois basin and its underlying crust. *Tectonophysics*, 363(1-2):45–78.

McGlannan, A. J. & Gilbert, H. (2016). Crustal signatures of the tectonic development of the north american midcontinent. *Earth and Planetary Science Letters*, 433:339–349.

McKenna, J., Stein, S., & Stein, C. A. (2007). Is the new madrid seismic zone hotter and weaker than its surroundings? *Special Papers-Geological Society of America*, 425:167.

Mei, S. & Kohlstedt, D. L. (2000). Influence of water on plastic deformation of olivine aggregates: 1. diffusion creep regime. *Journal of Geophysical Research: Solid Earth*, 105(B9):21457–21469.

Mooney, W., Andrews, M., Ginzburg, A., Peters, D., & Hamilton, R. (1983). Crustal structure of the northern mississippi embayment and a comparison with other continental rift zones. *Tectonophysics*, 94(1-4):327–348.

Mueller, K., Hough, S. E., & Bilham, R. (2004). Analysing the 1811–1812 new madrid earthquakes with recent instrumentally recorded aftershocks. *Nature*, 429(6989):284.

Niu, Y. (2005). Generation and evolution of basaltic magmas: some basic concepts and a new view on the origin of mesozoic–cenozoic basaltic volcanism in eastern china. *Geological Journal of China Universities*, 11(1):9–46.

Nyamwandha, C. A., Powell, C. A., & Langston, C. A. (2016). A joint local and teleseismic tomography study of the mississippi embayment and new madrid seismic zone. *Journal of Geophysical Research: Solid Earth*, 121(5):3570–3585.

Okure, M. S. & McBride, J. H. (2006). Deep seismic reflectivity beneath an intracratonic basin: Insights into the behavior of the uppermost mantle beneath the illinois basin. *Precambrian Research*, 149(3-4):99–125.

Peacock, S. M. et al. (2003). Thermal structure and metamorphic evolution of subducting slabs. *Geophysical Monograph-American Geophysical Union*, 138:7–22.

Pollitz, F., Kellogg, L., & Burgmann, R. (2001). Sinking mafic body in a reactivated lower crust: A mechanism for stress concentration at the new madrid seismic zone. *Bulletin of the Seismological Society of America*, 91(6):1882–1897.

Pollitz, F. F. & Mooney, W. D. (2014). Seismic structure of the central us crust and shallow upper mantle: Uniqueness of the reelfoot rift. *Earth and Planetary Science Letters*, 402:157–166.

Porritt, R. W., Allen, R. M., & Pollitz, F. F. (2014). Seismic imaging east of the rocky mountains with usarray. *Earth and Planetary Science Letters*, 402:16–25.

Ram´ırez-Guzm´an, L., Boyd, O. S., Hartzell, S., & Williams, R. A. (2012). Seismic velocity model of the central united states (version 1): Description and simulation of the 18 april 2008 mt. carmel, illinois, earthquake. *Bulletin of the Seismological Society of America*, 102(6):2622–2645.

Richard, G., Bercovici, D., & Karato, S.-I. (2006). Slab dehydration in the earth's mantle transition zone. *Earth and Planetary Science Letters*, 251(1-2):156–167.

Santosh, M., Zhao, D., & Kusky, T. (2010). Mantle dynamics of the paleoproterozoic north china craton: a perspective based on seismic tomography. *Journal of Geodynamics*, 49(1):39–53.

Saxena, A. (2020). *Investigating Intraplate Seismicity in the Central and Eastern US: Linking Observations and Numerical Models* (Doctoral dissertation, The University of Memphis).

Saxena, A., Choi, E., & Powell, C. A. (2017). Stress concentration on Intraplate Seismicity: Numerical Modeling of Slab-released Fluids in the New Madrid Seismic Zone. *AGUFM, 2017*, T54A-05.

Schmandt, B. & Lin, F.-C. (2014). P and s wave tomography of the mantle beneath the united states. *Geophysical Research Letters*, 41(18):6342–6349.

Schutt, D. & Lesher, C. (2006). Effects of melt depletion on the density and seismic velocity of garnet and spinel lherzolite. *Journal of Geophysical Research: Solid Earth*, 111(B5).

Schutt, D. L. & Lesher, C. E. (2010). Compositional trends among kaapvaal craton garnet peridotite xenoliths and their effects on seismic velocity and density. *Earth and Planetary Science Letters*, 300(3-4):367–373.

Sigloch, K. (2011). Mantle provinces under north america from multifrequency p wave tomography. *Geochemistry, Geophysics, Geosystems*, 12(2).

Sigloch, K., McQuarrie, N., & Nolet, G. (2008). Two-stage subduction history under north america inferred from multiple-frequency tomography. *Nature Geoscience*, 1(7):458–462.

Smith, D., Riter, J. A., & Mertzman, S. A. (1999). Water–rock interactions, orthopyroxene growth, and si-enrichment in the mantle: evidence in xenoliths from the colorado plateau, southwestern united states. *Earth and Planetary Science Letters*, 165(1):45–54.

Smyth, J. R., Holl, C. M., Frost, D. J., Jacobsen, S. D., Langenhorst, F., & Mccammon, C. A. (2003). Structural systematics of hydrous ringwoodite and water in earth's interior. *American Mineralogist*, 88(10):1402–1407.

915 Sobolev, S. V. & Babeyko, A. Y. (1994). Modeling of mineralogical composition, density and
916 elastic wave velocities in anhydrous magmatic rocks. *Surveys in geophysics*, 15(5):515–
917 544.

918 Sobolev, S. V., Zeyen, H., Stoll, G., Werling, F., Altherr, R., & Fuchs, K. (1996). Upper mantle
919 temperatures from teleseismic tomography of french massif central including effects of
920 composition, mineral reactions, anharmonicity, anelasticity and partial melt. *Earth and*
921 *Planetary Science Letters*, 139(1-2):147–163.

922 Tavakoli, B., Pezeshk, S., & Cox, R. T. (2010). Seismicity of the new madrid seismic zone
923 derived from a deep-seated strike-slip fault seismicity of the new madrid seismic zone
924 derived from a deep-seated strike-slip fault. *Bulletin of the Seismological Society of*
925 *America*, 100(4):1646–1658.

926 Thomas, W. A. et al. (2006). Tectonic inheritance at a continental margin. *GSA today*, *16*(2):4–
927 11.

928 Thomas, W. A. & Powell, C. A. (2017). Necessary conditions for intraplate seismic zones in
929 north america. *Tectonics*, 36(12):2903–2917.

930 Thybo, H., Perchu´c, E., & Zhou, S. (2000). Intraplate earthquakes and a seismically defined
931 lateral transition in the upper mantle. *Geophysical research letters*, 27(23):3953–3956.

932 Tian, Y. & Zhao, D. (2011). Destruction mechanism of the north china craton: insight from p and
933 s wave mantle tomography. *Journal of Asian Earth Sciences*, 42(6):1132–1145.

934 Wagner, L. S., Anderson, M. L., Jackson, J. M., Beck, S. L., & Zandt, G. (2008). Seismic
935 evidence for orthopyroxene enrichment in the continental lithosphere. *Geology*,
936 36(12):935– 938.

Whitmeyer, S. J. & Karlstrom, K. E. (2007). Tectonic model for the proterozoic growth of north america. *Geosphere*, 3(4):220–259.

Windley, B., Maruyama, S., & Xiao, W. (2010). Delamination/thinning of sub-continental lithospheric mantle under eastern china: The role of water and multiple subduction. *American Journal of Science*, 310(10):1250–1293.

Yang, X., Pavlis, G. L., Hamburger, M. W., Marshak, S., Gilbert, H., Rupp, J., Larson, T. H., Chen, C., & Carpenter, N. S. (2017). Detailed crustal thickness variations beneath the illinois basin area: Implications for crustal evolution of the midcontinent. *Journal of Geophysical Research: Solid Earth*, 122(8):6323–6345.

Yang, X., Pavlis, G. L., Hamburger, M. W., Sherrill, E., Gilbert, H., Marshak, S., Rupp, J., & Larson, T. H. (2014). Seismicity of the ste. genevieve seismic zone based on observations from the earthscope oiink flexible array. *Seismological Research Letters*, 85(6):1285–1294.

Yang, X.-Z., Xia, Q.-K., Deloule, E., Dallai, L., Fan, Q.-C., & Feng, M. (2008). Water in minerals of the continental lithospheric mantle and overlying lower crust: a comparative study of peridotite and granulite xenoliths from the north china craton. *Chemical Geology*, 256(1-2):33–45.

Zhan, Y., Hou, G., Kusky, T., & Gregg, P. M. (2016). Stress development in heterogenetic lithosphere: Insights into earthquake processes in the new madrid seismic zone. *Tectonophysics*, 671:56–62.

957 Zhang, Q., Sandvol, E., & Liu, M. (2009). Lithospheric velocity structure of the new madrid
958 seismic zone: A joint teleseismic and local p tomographic study. *Geophysical Research*
959 *Letters*, 36(11).

960 Zhao, D., Hasegawa, A., & Horiuchi, S. (1992). Tomographic imaging of p and s wave velocity
961 structure beneath northeastern japan. *Journal of Geophysical Research: Solid Earth*,
962 97(B13):19909–19928.

963 Zhao, D., Hasegawa, A., & Kanamori, H. (1994). Deep structure of japan subduction zone as
964 derived from local, regional, and teleseismic events. *Journal of Geophysical Research:*
965 *Solid Earth*, 99(B11):22313–22329.

966 Zhao, D., Kanamori, H., & Humphreys, E. (1996). Simultaneous inversion of local and
967 teleseismic data for the crust and mantle structure of southern california. *Physics of the*
968 *earth and planetary interiors*, 93(3-4):191–214.

969 Zhao, Y.-H., Zimmerman, M. E., & Kohlstedt, D. L. (2009). Effect of iron content on the creep
970 behavior of olivine: 1. anhydrous conditions. *Earth and Planetary Science Letters*, 287(1-
971 2):229–240.

972